

A MICRO-MACRO FRAMEWORK FOR ANALYZING STERIC AND HYDRODYNAMIC INTERACTIONS IN GLIDING ASSAYS*

STEVEN C. COOK[†], CHRISTEL HOHENEGGER[‡], AND TAMAR SHINAR[§]

Abstract.

Macroscopic flows of filament-motor mixtures, driven by the hydrolysis of ATP, are important to many cellular processes such as cytoplasmic streaming in *Drosophila* oocytes and cortical flow in the first cell division of *C. elegans*. Gliding assays, reduced *in vitro* model systems where motor proteins adsorbed onto a planar substrate bind to and move filaments, recreate large-scale dynamic patterns like coherent swarming motion and density waves. These systems are sensitive to the microscopic behavior such as the motor protein binding and unbinding dynamics, which take place on a faster timescale than the direct and fluid-mediated filament interactions. In this work, we present a multiscale modeling and simulation framework for gliding assays that allows detailed microscopic motor modeling as well as both steric and hydrodynamic interactions between filaments. Our model is based on continuum kinetic theory, and our implementation utilizes CPU and GPU parallelism to track the sparse but high-dimensional state space arising from the microscopic motor protein configurations. We find that steric interactions play a role in the formation of spatiotemporally coherent flow structures, and qualitatively reproduce experimentally observed behaviors including filament crossover and alignment, and clump formation, merging, and splitting.

Key words. micro-macro methods, multiscale simulation, gliding assay, cytoskeleton, motor proteins, active suspensions, hydrodynamics, solid-fluid coupling, steric interactions, heterogenous computing, emergent phenomena

AMS subject classifications. 76Z99, 76M20, 76M22, 92C05, 65C20, 68U20, 65Y05

1. Introduction. Actin and tubulin filaments working in concert with motor proteins play a central role in cell functions including mitosis and pronuclear centering [31]. Gliding assays, in which stabilized filaments are propelled by anchored motor proteins powered by the hydrolysis of ATP in a thin quasi-two-dimensional chamber, are commonly used to study the behavior of these cellular components *in vitro* (Figure 1). Large-scale pattern formation is observed in such experiments, including clump formation, merging, and splitting, and density waves [29], and the emergence of a lattice of microtubule vortices [32].

The physics of the filament-motor-fluid system are inherently multiscale in space and time, with nanoscale motors with fast binding/unbinding kinetics coupled to microscale filaments interacting in a macroscopic fluid domain. These systems have been studied with a variety of theoretical and computational approaches. Models that track explicit representations of filaments with Langevin dynamics underscore the sensitivity of the system to the motor behavior; [15, 14] included a load-dependent force-velocity relationship of motor proteins in a gliding assay and found that the motor activity increases nematic ordering, and [19, 22, 20] found that the time spent by individual motors at the end of a microtubule before falling off plays a central role in the emergence of coherent structures. These models neglect fluid-mediated filament-filament

*Submitted to the editors January 2017.

Funding: S.C. and T.S. were supported by the National Institute of General Medical Sciences of the National Institutes of Health under award R01GM104976. The content is solely the responsibility of the authors and does not necessarily represent the official views of the National Institutes of Health. T.S. was also supported by the Amrik Singh Poonian endowed chair at the University of California, Riverside.

[†]Department of Computer Science, UC Riverside, Riverside, CA (scook005@cs.ucr.edu).

[‡]Department of Mathematics, University of Utah, Salt Lake City, UT (choheneg@math.utah.edu).

[§]Department of Computer Science, UC Riverside, Riverside, CA (shinar@cs.ucr.edu).

41 interactions, and are therefore not suitable to address such behaviors. Moreover, the
 42 computations have scaled to only hundreds of filaments, while many systems of inter-
 43 est such as a mitotic spindle are estimated to have tens or hundreds of thousands of
 44 filaments. A model based on macroscopic configuration fields, and thus more suitable
 45 to a large system and large length and time scales, was proposed by [16]. This was
 46 expanded upon by [27] in a hydrodynamic theory incorporating explicit tracking of
 47 bound and unbound motor populations. Both [27, 16] rely on phenomenologically
 48 motivated constitutive equations in the model derivation and neglect filament density
 49 fluctuations. Another class of modeling approaches starts with a microscopic model
 50 and coarse-grains the system to attain a macroscopic description [18, 33, 1]. For ex-
 51 ample, [18] assume a constant motor density and demonstrate that inhomogeneities
 52 in motor stepping rate are necessary to drive bundle formations, and [33], without
 53 considering fluctuations in motors or filament densities, show that the order of the
 54 isotropic-nematic transition depends on the force-dependent motor detachment. How-
 55 ever, both of [33, 1] neglect fluid-mediated filament-filament interactions, although
 56 they could be coupled to the fluid equation using a configurational average of an ex-
 57 pression involving the distribution function to include the contribution of the particles
 58 to the fluid stress [4, 3]. This approach has been widely applied to nanorods [34], and
 59 more recently to active gels [17] and to suspensions of active swimmers [25, 26], and
 60 was used in our previous work [11]. Such methods have the benefit of flexibly allowing
 61 detailed microscopic modeling. However, it is not always possible to avoid tracking
 62 the microscopic variables, which can incur significant computational cost.

63 As shown experimentally by, among others, [29, 14, 32], the filament density and
 64 steric interactions play a critical role in the formation of coherent structures. In this
 65 paper we consider dense suspensions of filaments, and build upon our previous model
 66 [11] to include steric interactions between filaments. A widespread model of steric
 67 interaction is the excluded volume potential [4]. This model, widely used in liquid
 68 crystal theory [34, 18], has been adapted to active suspensions of self-propelled pushers
 69 and pullers in three dimensions [7]. The latter includes a rotational steric alignment
 70 term, but neglects the linear steric contribution which can prevent unphysical “piling
 71 up” amongst the microtubules in a gliding assay. We follow this approach to modeling
 72 steric interactions, including both rotational and linear steric interaction terms.

73 Characterizing the interplay of steric versus hydrodynamic effects requires an ex-
 74 ploration of different filament densities and motor systems. At a microtubule density
 75 of $.05\mu\text{m}^{-2}$, Sumino et al. [32] are able to model their experimentally observed vortex
 76 lattice with a phenomenological agent-based method neglecting hydrodynamics. In
 77 contrast, at actomyosin surface densities ranging between $2\mu\text{m}^{-2}$ to $21\mu\text{m}^{-2}$, Schaller
 78 et al. [29] demonstrate filament clump and density wave persistence and scale that
 79 cannot be explained through purely steric interactions. Additionally, Schaller et al.
 80 [28] demonstrate evidence of hydrodynamic effects in the formation of depletion layers
 81 between clump-clump or clump-wall collisions that cause reorientation before physical
 82 contact. The particulars of the microscopic motors may also significantly influence
 83 the collective motion. For example, [32] reports that using kinesin motor proteins
 84 instead of dynein results in a higher rate of microtubule crossover events, limiting
 85 steric interactions and preventing the formation of the vortex lattice. The impor-
 86 tance of fluid effects can also be seen further in the theoretical study of filaments in a
 87 quasi-two-dimensional chamber [10].

88 In this work, we present a novel micro-macro model and computational framework
 89 to simulate both steric and hydrodynamic interactions in a microtubule gliding assay.
 90 Our new framework supports different motor protein activity models, as well as the

91 option to treat the filaments as self-propelled. Rather than use phenomenological
 92 steric interaction rules, we model fluid stresses due to microtubule inextensibility,
 93 rotational and translational steric interactions, and self-propulsion if applicable.

94 We base our approach on our previous work [11], where we developed a contin-
 95 uum model coupling the motion of the fluid to the motion of the motors and micro-
 96 tubules. In that work, we used closure approximations to reduce the fluid equations
 97 to depth-averaged two-dimensional equations, and restricted ourselves to the dilute
 98 limit, ignoring steric interactions. Here, we solve the fluid equations in three dimen-
 99 sions and avoid making closure approximations. As in [11], we track distributions
 100 of microtubules and kinesin motor proteins, with behavior governed by conservation
 101 equations.

102 The paper is organized as follows. Our framework is presented in Section 2, the
 103 implementation and numerical methods are presented in Section 3, simulation results
 104 are presented in Section 4, and we conclude in Section 5.

105 2. Modeling framework.

106 This section reviews the setup of a gliding motility assay, describes our continuous
 107 representation, and details the individual components of our modeling framework.
 108 Two distributions are tracked: one for the microtubules, and one for the bound mo-
 109 tors. Each distribution satisfies a conservation equation. We present one such equa-
 110 tion for the microtubule distribution taking into account hydrodynamic and steric
 111 effects, and two for the bound motor distribution. Bulk fluid forces and steric stresses
 112 are calculated from the bound motor proteins and the microtubule distribution re-
 113 spectively, and included in the fluid equations.

114 2.1. Microscale model.

115 Figure 1 illustrates the experimental setup. A microtubule gliding assay consists
 116 of two plates separated by a small distance. A fluid fills the gap, with fluid flow
 117 characterized by low Reynolds number. Motor proteins (kinesin in our case) are
 118 anchored to the bottom plate with their heads free to bind to microtubules, walk
 119 along them, and detach. The microtubules, in turn, glide along the motor protein
 120 heads, effectively constrained within a single plane. They are stabilized to prevent
 121 growth or depolymerization, and have an orientation defined in terms of a plus and
 122 minus end. Upon binding, kinesin motor proteins walk towards the plus end of the
 123 microtubule, propelling the microtubule in the direction of its minus end. We assume
 124 ATP saturation so the motor proteins are continuously active. We refer the reader to
 125 [11] for a list of values of physical parameters found in the literature.

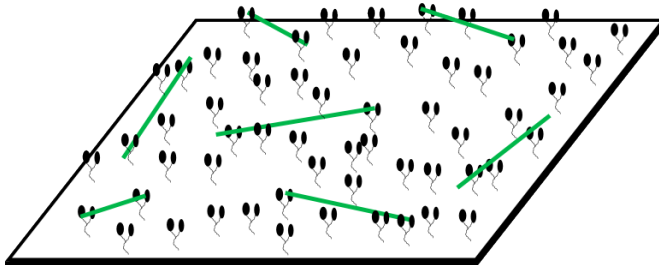


Fig. 1: Microtubule gliding assay setup. Motor protein (black) tails are anchored to a fixed plate, while their heads bind and pull microtubules (green).

126 **2.1.1. Microtubule distribution.** In this model, we assume that the micro-
 127 tubules of length $2l$ and diameter b are inextensible and rigid, an appropriate ap-
 128 proximation for microtubules of $l \leq 2\mu m$ [30]. We describe the microtubules by the
 129 position of their center-of-mass \mathbf{x} and a vector \mathbf{p} pointed towards their plus end.
 130 Let $\Psi(\mathbf{x}, \mathbf{p}, t)$ be the microtubule distribution function. Ψ evolves according to the
 131 Smoluchowski equation (see also [12, 11])

$$\begin{aligned}
 132 \quad (1) \quad & \partial_t \Psi + \nabla_x \cdot (\dot{\mathbf{x}}\Psi) + \nabla_p \cdot (\dot{\mathbf{p}}\Psi) = 0 \\
 133 \quad (2) \quad & \dot{\mathbf{x}}_2 = -V_{\text{sp}}\mathbf{p}_2 + \mathbf{u}_2(\mathbf{x}) - \nabla_{x_2} U_t - D_{t,\parallel} \nabla_{x_2} \ln \Psi, \\
 134 \quad (3) \quad & \dot{z} = w(\mathbf{x}) - \partial_z U_t - D_{t,\perp} \partial_z \ln \Psi \\
 135 \quad (4) \quad & \dot{\mathbf{p}} = (\mathbf{I} - \mathbf{p}\mathbf{p})\nabla_x \mathbf{u}(\mathbf{x})\mathbf{p} - \nabla_p U_r - D_r \nabla_p \ln \Psi.
 \end{aligned}$$

Here the subscript 2 denotes the in-plane x, y components and derivatives with respect to these variables. The first two and last terms in the equations for $\dot{\mathbf{x}} = (\dot{\mathbf{x}}_2 \dot{z})^T$ and $\dot{\mathbf{p}}$ are similar to those of the active bacteria swimming model of [26]. V_{sp} is a propulsion velocity, analogous to the self-propulsion term in active swimmer models. Since microtubules do not propel themselves through the fluid as a bacteria does [28], but are propelled by motors, the resulting force should act like a monopole (see Eqs. (15)-(16)), similar to sedimenting particles [5]. Therefore, we include both a self-propulsion velocity and a passive force in our model. Furthermore, $\mathbf{u}(\mathbf{x}) = (\mathbf{u}_2(\mathbf{x}) w(\mathbf{x}))^T$ is the velocity of the surrounding fluid at \mathbf{x} with which the microtubules are advected. Because the kinesin motors walk towards the plus end, i.e. in the direction of \mathbf{p} , the microtubule will move in the direction $-\mathbf{p}_2$ in the plane of motion where it is restricted. $D_{t,\parallel}$, $D_{t,\perp}$ and D_r are the translational and rotational diffusion coefficients, respectively. Because of the channel geometry and the experimental observation that microtubules move in a z -plane, we expect $D_{t,\perp}$, the diffusion in the z direction, to be smaller than the in-plane diffusion $D_{t,\parallel}$. We use zero diffusion in all of our examples. We do not include thermal fluctuations in the present model. The third term in $\dot{\mathbf{x}}_2$ and $\dot{\mathbf{p}}$ and the second term in \dot{z} describes the effect of steric interactions through a translational and rotational potential, $U_{t/r}$, respectively. We model the steric potential using the Maier-Saupe potential $K_{t/r}(\mathbf{p}, \mathbf{p}') = -U_{t/r}^0 (\mathbf{p} \cdot \mathbf{p}')^2$ with

$$U_{t/r}(\mathbf{x}, \mathbf{p}, t) = \int \Psi(\mathbf{x}, \mathbf{p}', t) K_{t/r}(\mathbf{p}, \mathbf{p}') d\mathbf{p}'.$$

137 The above form of U_r is identical to the one proposed by [7] for active suspension, but
 138 we also keep the translational steric potential U_r from [18] to prevent interpenetration
 139 in the plane of the microtubules. With the previous definitions of the steric potential
 140 the translational and rotational fluxes become

$$\begin{aligned}
 141 \quad (5) \quad & \dot{\mathbf{x}}_2 = -V_{\text{sp}}\mathbf{p}_2 + \mathbf{u}_2(\mathbf{x}) + U_{t,\parallel}^0 \mathbf{p}\mathbf{p} : \nabla_2 \mathbf{D}(\mathbf{x}, t) - D_{t,\parallel} \nabla_2 \ln \Psi \\
 142 \quad (6) \quad & \dot{z} = w(\mathbf{x}) + U_{t,\perp}^0 \mathbf{p}\mathbf{p} : \partial_z \mathbf{D}(\mathbf{x}, t) - D_{t,\perp} \partial_z \ln \Psi \\
 143 \quad (7) \quad & \dot{\mathbf{p}} = (\mathbf{I} - \mathbf{p}\mathbf{p})(\nabla_x \mathbf{u}(\mathbf{x}) + 2U_r^0 \mathbf{D}(\mathbf{x}, t))\mathbf{p} - D_r \nabla_p \ln \Psi,
 \end{aligned}$$

145 where $\mathbf{D}(\mathbf{x}, t) = \int \Psi(\mathbf{x}, \mathbf{p}, t) \mathbf{p}\mathbf{p} d\mathbf{p}$ is the second moment of Ψ with respect to \mathbf{p} . The
 146 total number of microtubules is given by $N = \iint \Psi d\mathbf{x} d\mathbf{p}$.

147 **2.1.2. Motor distributions.** In general, the free and bound motor populations
 148 evolve according to a reaction-diffusion-advection equation. In a gliding assay, motor
 149 tails are fixed to a plate and cannot diffuse or advect with the flow. Hence, we consider

150 only the conversion between the free and bound populations, and the advection and
 151 procession of the bound motor heads. We represent the free motor density as $\mathcal{M}_f(\mathbf{r}_0)$,
 152 the density of motors with free heads and tails anchored at position \mathbf{r}_0 . We do not
 153 track the position of free motor heads. We represent the bound motor density per mi-
 154 crotubule as $\mathcal{M}_b(\mathbf{r}_0, s | (\mathbf{x}, \mathbf{p}), t)$, with \mathbf{r}_0 the position where the motor tail is anchored,
 155 $\mathbf{x}, s, \mathbf{p}$ the center of mass, arclength parameter, and orientation of the microtubule
 156 the motor head is bound to, and t the time. The notation $|(\mathbf{x}, \mathbf{p})$ denotes that the
 157 probability is conditional on the distribution of microtubules $\Psi(\mathbf{x}, \mathbf{p}, t)$. Finally, we
 158 let $\mathcal{M}(\mathbf{r}_0)$ be the total (bound + free) motor density at \mathbf{r}_0 . We define the free motor
 159 density \mathcal{M}_f as

$$160 \quad (8) \quad \mathcal{M}_f(\mathbf{r}_0, t) = \mathcal{M}(\mathbf{r}_0) - \iiint \mathcal{M}_b(\mathbf{r}_0, s | (\mathbf{x}, \mathbf{p}), t) \Psi(\mathbf{x}, \mathbf{p}, t) ds d\mathbf{x} d\mathbf{p},$$

162 that is, for every motor with tail anchored at \mathbf{r}_0 the head is either free or bound. The
 163 total number of bound motors is given by $N_b = \iiint \mathcal{M}_b \Psi d\mathbf{r}_0 d\mathbf{x} d\mathbf{p} ds$. In the entire
 164 system, the total number of motors $N_m = N_f + N_b$ is constant.

165 The possible configurations of bound motor heads face constraints. First, a head
 166 detaches if it walks off the plus end of the microtubule ($|s| > l$). Second, the motor
 167 head detaches due to stretching of the motor stalk, which happens beyond a critical
 168 distance r_c . We do not model the spring force of the motor stalk extension. We
 169 enforce these two constraints by requiring that \mathcal{M}_b is zero when $|s| > l$ and by taking
 170 \mathcal{M}_b to be zero when $|\mathbf{x} + s\mathbf{p} - \mathbf{r}_0| \geq r_c$. Equivalently, the second condition says that
 171 for a given tail \mathbf{r}_0 there is only a small subset of $\mathbf{x} + s\mathbf{p}$ available for attachment. This
 172 crucial locality restriction effectively reduces the dimensionality of \mathcal{M}_b . We represent
 173 the allowable local configurations as a ball of radius r_c illustrated in Figure 2,

$$174 \quad (9) \quad B_{r_c}(\mathbf{r}_0) = \{(\mathbf{x}', s', \mathbf{p}') : |\mathbf{x}' + s'\mathbf{p}' - \mathbf{r}_0| < r_c\}.$$

176 We consider two equations for the bound mo-
 177 tor distribution. The first, hereafter referred to
 178 as the “evolved” model, tracks \mathcal{M}_b through the
 179 evolution of a full conservation equation. It mod-
 180 els motor head stepping along microtubules as
 181 well as attachment proportional to the available
 182 number and length of microtubules and detach-
 183 ment. Since motors bind and unbind quickly rel-
 184 ative to the speed of the microtubules, this con-
 185 servation equation has its own smaller timescale.
 186 The second model, hereafter referred to as the
 187 “simplified” model, assumes that motors bind to
 188 any reachable position s along a microtubule with
 189 equal probability, and that the distribution of
 190 bound motors $\mathcal{M}_b \Psi$ with tails anchored at \mathbf{r}_0
 191 is proportional to the density of microtubules to
 192 bind to up until all available motors are bound. The fidelity of the smaller timescale
 193 behavior from the evolved motor model is lost. Instead of solving a conservation
 194 equation at a separate timescale, \mathcal{M}_b is updated from Ψ on its timescale.

195 In the evolved motor model, following [21], the number of binding events per
 196 second is proportional to the local density of free motors times the available length of
 197 microtubules (as an approximation for the available binding sites) with the constant

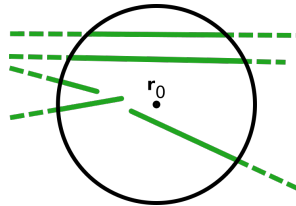


Fig. 2: Set $B_{r_c}(\mathbf{r}_0)$ of microtubule segments accessible to motor head for motor tail anchored at \mathbf{r}_0 in solid green (illustrated in 2D for clarity).

198 of proportionality, denoted by $\overline{k_{\text{on}}}$, that has units of $\mu m^2 s^{-1}$. Defining $\bar{B}(\mathbf{r}_0) =$
 199 $\iiint_{B_{r_c}} \Psi \mathcal{M}_b ds dx d\mathbf{p}$, then $\bar{B}(\mathbf{r}_0)$ represents the number of bound motors in B_{r_c} per
 200 unit area. Since \bar{B} and \mathcal{M}_f have units of number per unit area (and not per unit
 201 volume), we divide $\overline{k_{\text{on}}}$ by the capture radius r_c to obtain a constant of proportionality
 202 that has units of $\mu m s^{-1}$, before repeating the argument of [21] for \bar{B} . In order to
 203 convert from a number per area to a number, we multiply $\bar{B}(\mathbf{r}_0)$ by the area of the
 204 disk D_{r_c} of radius r_c centered at \mathbf{r}_0 . Therefore, after dividing through by $|D_{r_c}|$ and
 205 neglecting advection terms, we have a relationship of the form

$$206 \quad \partial_t \bar{B} = -k_{\text{off}} \bar{B} + \frac{\overline{k_{\text{on}}}}{r_c |D_{r_c}|} \mathcal{M}_f \iiint_{B_{r_c}} \Psi dx d\mathbf{p} ds,$$

207 where the integral of Ψ over B_{r_c} represents the total length of available microtubules
 208 and k_{off} (units of s^{-1}) is the detachment rate. Setting $k_{\text{on}} = \overline{k_{\text{on}}}/(r_c |D_{r_c}|)$ with units
 209 of $(\mu m s)^{-1}$ and including advection terms, the conservation equation for $\mathcal{M}_b \Psi$ is

$$210 \quad (10) \quad \begin{aligned} \partial_t (\mathcal{M}_b \Psi) + \partial_s (V_m \mathcal{M}_b \Psi) + \nabla_x \cdot (\dot{\mathbf{x}} \mathcal{M}_b \Psi) + \nabla_p \cdot (\dot{\mathbf{p}} \mathcal{M}_b \Psi) \\ = k_{\text{on}} \Psi \mathcal{M}_f \mathbb{1}_{B_{r_c}(\mathbf{r}_0)} - k_{\text{off}} \mathcal{M}_b \Psi. \end{aligned}$$

211 Here $\mathbb{1}_{B_{r_c}(\mathbf{r}_0)}$ is the indicator function for $B_{r_c}(\mathbf{r}_0)$. The flux terms on the left hand
 212 side express the procession of the motor along the microtubule with speed V_m and
 213 the motion of the motor-microtubule complex with the background flow. The source
 214 terms on the right hand side express the attachment of a free motor at s to the
 215 microtubule \mathbf{x}, \mathbf{p} at a rate per length k_{on} , and the detachment of a bound motor at a
 216 rate k_{off} . Using Eq. (1) to eliminate Ψ , Eq. (10) simplifies to

$$217 \quad (11) \quad [\partial_t \mathcal{M}_b + \partial_s (V_m \mathcal{M}_b) + \dot{\mathbf{x}} \cdot \nabla_x \mathcal{M}_b + \dot{\mathbf{p}} \cdot \nabla_p \mathcal{M}_b] \Psi = k_{\text{on}} \mathcal{M}_f \Psi \mathbb{1}_{B_{r_c}} - k_{\text{off}} \mathcal{M}_b \Psi.$$

218 We note that if $\Psi \neq 0$ for all $(\mathbf{x}, \mathbf{p}, t)$ we can divide by Ψ , but we will refrain from
 219 doing so until Section 2.2.

220 In this paper, we also consider a simplified heuristic motor model where all motor
 221 heads are located in the same plane at height z_0 and the number of bound motors
 222 is proportional to the number of microtubules available within the binding range.
 223 Therefore, we let \mathcal{M}_b be the piecewise function

$$224 \quad (12) \quad \mathcal{M}_b(\mathbf{r}_0, s | (\mathbf{x}, \mathbf{p}), t) = \begin{cases} 0 & \text{if } |\mathbf{x} + s\mathbf{p} - \mathbf{r}_0| \geq r_c \\ \min \left(C, \frac{\mathcal{M}(\mathbf{r}_0)}{\iiint_{B_{r_c}} \Psi dx d\mathbf{p} ds} \right) & \text{if } |\mathbf{x} + s\mathbf{p} - \mathbf{r}_0| < r_c \end{cases}.$$

225 In the above, the cutoff constant C has the same units as \mathcal{M}_b . The second term in the
 226 minimum effectively caps \mathcal{M}_b so that $\iiint_{B_{r_c}} \mathcal{M}_b \Psi dx ds d\mathbf{p} \leq \mathcal{M}$, the total available
 227 motors at \mathbf{r}_0 . Above the threshold value C , all local motor heads are bound. As C
 228 increases, so do the number of bound motors at \mathbf{r}_0 for a fixed value of $\iiint_{B_{r_c}} \Psi dx ds d\mathbf{p}$,
 229 so larger C values decrease the minimum rod density needed to bind all local motors.

230 **2.1.3. Fluid.** The bulk fluid motion is described by the incompressible Stokes
 231 equations for low Reynolds number flows with suspended microtubule and motor
 232 microstructure. As is customary [2], the total stress in the fluid can be divided into
 233 a Newtonian stress and an extra stress arising from the microstructure, leading to

$$234 \quad (13) \quad -\mu \nabla_{\mathbf{x}}^2 \mathbf{u}(\mathbf{x}) + \nabla_{\mathbf{x}} q(\mathbf{x}) = \nabla_{\mathbf{x}} \cdot \boldsymbol{\sigma}^p(\mathbf{x}) + \mathbf{f}_m(\mathbf{x}), \quad \nabla_{\mathbf{x}} \cdot \mathbf{u}(\mathbf{x}) = 0.$$

236 In the above, q is the pressure, μ is the dynamic viscosity, $\boldsymbol{\sigma}^p$ is the extra stress, and
 237 \mathbf{f}_m is the force density due to the motors acting at \mathbf{x} on the immersed microtubules.
 238 We take the fluid domain to be doubly periodic in x, y with no-slip conditions at the
 239 plate $z = -H/2$ and at the cover slip $z = H/2$.

240 We define the extra stress as $\boldsymbol{\sigma}^p = \boldsymbol{\sigma}^f + \boldsymbol{\sigma}^t$ similar to [7], where $\boldsymbol{\sigma}^f$ arises from
 241 microtubules inextensibility and $\boldsymbol{\sigma}^t$ arises from steric interaction in $\dot{\mathbf{p}}$. These extra
 242 stresses are

$$243 \quad (14) \quad \boldsymbol{\sigma}^f = \sigma_f \mathbf{S} : \mathbf{E}, \quad \boldsymbol{\sigma}^t = -\sigma_t [\mathbf{D} \cdot \mathbf{D} - \mathbf{S} : \mathbf{D}],$$

244 where $\mathbf{E}(\mathbf{x}, t) = \frac{1}{2} (\nabla \mathbf{u} + \nabla \mathbf{u}^T)$ is the rate-of-strain tensor and \mathbf{S} is the fourth order
 245 moment of Ψ , $\mathbf{S}(\mathbf{x}, t) = \int \Psi \mathbf{p} \mathbf{p} \mathbf{p} \mathbf{p} d\mathbf{p}$. The coefficients are $\sigma_f = \pi \mu 4l^3 / 3 \ln(2r)$ and
 246 $\sigma_t = \pi \mu 8l^3 U_r^0 / 3 \ln(2r)$, which can be derived using slender body theory (see [7, 26]
 247 for details). We remark that steric interaction in space does not lead to extra stress terms
 248 in the slender body framework as the resulting force is constant along the microtubule.

249 In this model, since we assume that the microtubules are passively advected by
 250 the fluid, we apply the force spreading approach of the immersed boundary method
 251 (see [23]) to our polymeric fluid to obtain the motor force [3]

$$252 \quad (15) \quad \mathbf{f}_m(\mathbf{x}, t) = \iiint \mathbf{F}(\mathbf{y}, s, \mathbf{p}, \mathbf{r}_0) \delta(\mathbf{y} + s\mathbf{p} - \mathbf{x}) \Psi(\mathbf{y}, \mathbf{p}, t) \mathcal{M}_b(\mathbf{r}_0, s | (\mathbf{y}, \mathbf{p}), t) ds d\mathbf{r}_0 d\mathbf{y} d\mathbf{p},$$

253 where \mathbf{F} is the force associated with a single motor. Further, we note that the convo-
 254 lution with the δ -Dirac function converts from the center-of-mass based description
 255 of Ψ to the spatial description of the force density. The force generated by all bound
 256 motor heads acting at $\mathbf{y} + s\mathbf{p}$ is spread to \mathbf{x} by integrating over all possible motor
 257 configurations with head at $\mathbf{y} + s\mathbf{p}$. In general motor stepping speed is load-dependent
 258 [13]. However, here we assume that the motor is stepping at a constant speed V_m ,
 259 where its max stepping speed is V_{\max} , and thus exerts a constant force of magnitude
 260 $F_{\text{st}}(1 - \frac{V_m}{V_{\max}})$ in $-\mathbf{p}$, with F_{st} the motor stall force. This gives the simplified expression
 261 for the motor force

$$262 \quad (16) \quad \mathbf{F}(\mathbf{y}, s, \mathbf{p}, \mathbf{r}_0) = \mathbf{F}(\mathbf{p}) = -F_{\text{st}} \left(1 - \frac{V_m}{V_{\max}} \right) \mathbf{p}.$$

263 2.2. Two-dimensional reduction.

264 Since the microtubules and bound motor heads are restricted to a two-dimensional
 265 plane of motion [24], the forcing term in the fluid equations can also be localized to
 266 that plane. Taking advantage of this fact obviates the need to track Ψ and \mathcal{M}_b in the
 267 z -dimension, which provides critical memory and computation savings when storing
 268 and solving for the two distributions.

269 **2.2.1. Microtubule distribution.** The microtubules are centered around a
 270 plane $z = z_0$, where z_0 is about the length of the motor protein, above the bottom
 271 plate

$$272 \quad (17) \quad \Psi(\mathbf{x}, \mathbf{p}, t) = \Psi_{z_0}(\mathbf{x}_2, \mathbf{p}, t) \delta_a(z - z_0).$$

273 Here δ_a is a smooth delta function, chosen to be

$$274 \quad (18) \quad \delta_a(z - z_0) = \begin{cases} \frac{1}{2a} (1 + \cos(\frac{\pi(z-z_0)}{a})) & |z - z_0| \leq a \\ 0 & |z - z_0| > a \end{cases}.$$

275 We remark that to prevent the presence of microtubules or motors at the top or
 276 bottom plates of the assay, we further require that $z_0 - a > \frac{-H}{2}$ and $z_0 + a < \frac{H}{2}$.
 277 We also introduce the notation $A_i = \int \delta_a^i(z - z_0) dz$ to denote the moments of δ_a . By
 278 construction, we have $A_1 = 1$, $A_2 = 3/(4a)$ and $A_3 = 5/(6a)$. Next, the microtubules
 279 are constrained to the plane given the geometry of the assay, so $\mathbf{p} = (\cos \theta, \sin \theta, 0)^T$.
 280 Defining $\mathbf{p}_2 = (\cos \theta, \sin \theta)^T$, we have the decomposition $\Psi_{z_0}(\mathbf{x}_2, \mathbf{p}, t) = \Psi_{z_0}(\mathbf{x}_2, \mathbf{p}_2, t)$.
 281 Using Eq. (17), the microtubule reduction proceeds by integrating Eq. (1) with
 282 respect to z . We use a bar to denote the integral over z of a quantity weighted by
 283 the smooth delta function, for example $\bar{\mathbf{u}}(\mathbf{x}_2) = \int \mathbf{u}(\mathbf{x}_2, z) \delta_a(z) dz$. Plugging Eq. (17)
 284 into Eqs. (1) and (5)-(7), integrating over z , and using the facts that $\nabla_p = \mathbf{p}_2^\perp \partial_\theta$ and
 285 that both w and δ_a vanish at the top and bottom plate, we obtain

$$286 \quad (19) \quad \partial_t \Psi_{z_0} + \nabla_2 \cdot (\bar{\dot{\mathbf{x}}}_2 \Psi_{z_0}) + \partial_\theta (\dot{\theta} \Psi_{z_0}) = 0,$$

287 where we have defined the quantities $\bar{\dot{\mathbf{x}}}_2$ and $\dot{\theta}$ as

$$288 \quad (20) \quad \bar{\dot{\mathbf{x}}}_2 = -V_{\text{sp}} \mathbf{p}_2 + \bar{\mathbf{u}}_2 + A_2 U_{t,\parallel}^0 \mathbf{p}_2 \mathbf{p}_2 : \nabla_2 \mathbf{D}_{2,z_0} - D_{t,\parallel} \nabla_2 \ln \Psi_{z_0}$$

$$289 \quad (21) \quad \dot{\theta} = (\nabla_2 \bar{\mathbf{u}}_2 + 2U_r^0 A_2 \mathbf{D}_{2,z_0}) : \mathbf{p}_2^\perp \mathbf{p}_2 - D_r \partial_\theta \ln \Psi_{z_0}.$$

291 **2.2.2. Bound motor distribution.** We make the same assumptions for the
 292 bound motor distribution, since the bound motor heads must be in plane with the
 293 microtubules they are bound to and write \mathcal{M}_b analogously to (17) as

$$294 \quad (22) \quad \mathcal{M}_b(\mathbf{r}_0, s | (\mathbf{x}, \mathbf{p}), t) = \mathcal{M}_{b,z_0}(s, \mathbf{r}_0 | \mathbf{x}_2, \theta, t) \delta_a(z - z_0).$$

296 To derive a reduced equation for the evolved bound motor distribution, we plug in the
 297 assumptions (22) and (17) into equation (11), integrate with respect to z and divide
 298 by Ψ_{z_0} . Noting that the set $B_{r_c}(\mathbf{r}_0)$ can be approximated as

$$299 \quad B_{r_c}(\mathbf{r}_0) \approx \left\{ (\mathbf{x}, s, \mathbf{p}) : (\mathbf{x}_2, s, \mathbf{p}_2) \in D_{r_c}(\mathbf{r}_0) \text{ and } -\frac{H}{2} \leq z \leq -\frac{H}{2} + d_{r_c}(\mathbf{x}_2, s, \theta) \right\},$$

300 where $D_{r_c}(\mathbf{r}_0) = \{(\mathbf{x}_2, s, \theta) : |\mathbf{x}_2 + s \mathbf{p}_2 - \mathbf{r}_0| < r_c\}$ is the disk of capture radius r_c and
 301 $d_{r_c}(\mathbf{x}_2, s, \theta) = \sqrt{r_c^2 - |\mathbf{x}_2 + s \mathbf{p}_2 - \mathbf{r}_0|^2}$, we find

$$302 \quad (23) \quad \begin{aligned} & \partial_t (\mathcal{M}_{b,z_0}) + \partial_s (V_m \mathcal{M}_{b,z_0}) + \bar{\dot{\mathbf{x}}}_2 \cdot \nabla_2 \mathcal{M}_{b,z_0} - \dot{\zeta} \mathcal{M}_{b,z_0} + \dot{\theta} \partial_\theta \mathcal{M}_{b,z_0} \\ & = -k_{\text{off}} \mathcal{M}_{b,z_0} + \frac{k_{\text{on}}}{A_2} \mathcal{M}_f B_2 \mathbb{1}_{D_{r_c}}. \end{aligned}$$

303 In (23), we defined the tilde quantities similarly to the bar quantities in (20)-(21), but
 304 with respect to δ_a^2 as opposed to δ_a . We have

$$305 \quad (24) \quad \dot{\bar{\mathbf{x}}}_2 = -V_{\text{sp}} \mathbf{p}_2 + \frac{1}{A_2} \bar{\mathbf{u}}_2 + \frac{A_3}{A_2} U_{t,\parallel}^0 \mathbf{p}_2 \mathbf{p}_2 : \nabla_2 \mathbf{D}_{2,z_0} - D_{t,\parallel} \nabla_2 \ln \Psi_{z_0}$$

$$306 \quad (25) \quad \dot{\zeta} = \frac{1}{2A_2} \widetilde{\partial_z w} - \frac{B_1}{A_2} U_{t,\perp}^0 \mathbf{p}_2 \mathbf{p}_2 : \mathbf{D}_{2,z_0}$$

$$307 \quad (26) \quad \dot{\theta} = \left(\frac{1}{A_2} \nabla_2 \bar{\mathbf{u}}_2 + 2U_r^0 \frac{A_3}{A_2} \mathbf{D}_{2,z_0} \right) : \mathbf{p}_2^\perp \mathbf{p}_2 - D_r \partial_\theta \ln \Psi_{z_0}.$$

309 The constants B_1 and B_2 are

$$310 \quad B_1 = \frac{1}{2} \int \delta_a^2(z - z_0) \partial_{zz} \delta_a(z - z_0) dz = -\frac{\pi^2}{4a^4} \quad B_2 = \int_{-H/2}^{-H/2 + d_{r_c}(\mathbf{x}_2, s, \theta)} \delta_a(z - z_0) dz.$$

311 While the quantity B_2 is a function of \mathbf{x}_2, s, θ , plugging Eq. (18) for δ_a into B_2 , inte-
 312 grating and using a Taylor series expansion of sine, yield $0 \leq B_2 \leq r_c/a$. Therefore,
 313 for the remainder of this paper, we let $B_2 = r_c/a$.

314 Following the same steps for the simplified motor model, we have

$$315 \quad (27) \quad \mathcal{M}_{b,z_0}(\mathbf{r}_0, s | (\mathbf{x}_2, \theta), t) = \begin{cases} 0 & \text{if } (\mathbf{x}_2, s, \theta) \notin D_{r_c} \\ H \min \left(C, \frac{\mathcal{M}(\mathbf{r}_0)}{\iiint_{D_{r_c}} \Psi_{z_0} d\mathbf{x}_2 d\theta ds} \right) & \text{if } (\mathbf{x}_2, s, \theta) \in D_{r_c} \end{cases}.$$

316 **2.2.3. Fluid.** While we do not average the fluid equations over z , some of the
 317 stress and force components are zero as a result of the two-dimensional reduction of
 318 \mathcal{M}_b and Ψ . As the stresses are defined in terms of moments of Ψ with respect to \mathbf{p} ,
 319 the implications of Eq. (17) for the stress tensors in (14) are

$$320 \quad (28) \quad \boldsymbol{\sigma}^f = \sigma_f \mathbf{S}_{z_0}(\mathbf{x}_2, t) : \mathbf{E}(\mathbf{x}, t) \delta_a(z - z_0)$$

$$321 \quad (29) \quad \boldsymbol{\sigma}^t = -\sigma_t (\mathbf{D}_{z_0}(\mathbf{x}_2, t) \cdot \mathbf{D}_{z_0}(\mathbf{x}_2, t) - \mathbf{S}_{z_0}(\mathbf{x}_2, t) : \mathbf{D}_{z_0}(\mathbf{x}_2, t)) \delta_a^2(z - z_0),$$

where we defined

$$\mathbf{D}_{z_0}(\mathbf{x}_2, t) = \int \Psi_{z_0}(\mathbf{x}_2, \theta, t) \mathbf{p} \mathbf{p} d\theta \quad \text{and} \quad \mathbf{S}_{z_0}(\mathbf{x}_2, t) = \int \Psi_{z_0}(\mathbf{x}_2, \theta, t) \mathbf{p} \mathbf{p} \mathbf{p} \mathbf{p} d\theta.$$

323 We note that the third row and column of $\boldsymbol{\sigma}^f, \boldsymbol{\sigma}^t$ are identically zero because the
 324 z -component of \mathbf{p} is zero. Therefore, we use the subscript 2 to denote the upper 2x2
 325 block of each tensor, such as \mathbf{D}_{2,z_0} . Since the motor force $\mathbf{F}(\mathbf{p})$ in Eq. (16) is in the
 326 direction $-\mathbf{p}$, the z -component of \mathbf{f}_m is zero. As a result, the fluid equations (13) take
 327 the form

$$328 \quad (30) \quad -\mu \nabla_2^2 \mathbf{u}_2(\mathbf{x}) - \mu \partial_{zz} \mathbf{u}_2(\mathbf{x}) + \nabla_2 q(\mathbf{x}) = \nabla_2 \cdot \boldsymbol{\sigma}_2^p(\mathbf{x}) + \mathbf{f}_2(\mathbf{x})$$

$$329 \quad (31) \quad -\mu \nabla_2^2 w(\mathbf{x}) - \mu \partial_{zz} w(\mathbf{x}) + \partial_z q(\mathbf{x}) = 0$$

$$330 \quad (32) \quad \nabla_2 \cdot \mathbf{u}_2(\mathbf{x}) + \partial_z w(\mathbf{x}) = 0$$

332 with

$$333 \quad \mathbf{f}_2(\mathbf{x}) = -F_{st} \left(1 - \frac{V_m}{V_{\max}} \right) \delta_a(z - z_0)^2 \iiint \mathbf{p}_2 \delta(\mathbf{y}_2 + s\mathbf{p}_2 - \mathbf{x}_2) \Psi_{z_0} M_{b,z_0} ds d\mathbf{r}_0 d\mathbf{y}_2 d\theta.$$

334 **2.3. Nondimensionalization.** In this section, we nondimensionalize the set
 335 of reduced equations introduced in Section 2.2. To do so, we first introduce the
 336 characteristic scales. Let the characteristic length be L in the x, y dimensions and
 337 $H = \varepsilon L$ in the z dimension ($\varepsilon \ll 1$), let the characteristic velocity be U in the x, y
 338 dimensions and W in the z dimension, and let the characteristic fluid time scale be
 339 $T = L/U$. We set

$$340 \quad \mathbf{x}_2 = L\mathbf{x}', \quad z = \varepsilon Lz' = Hz', \quad \mathbf{u}_2 = U\mathbf{u}', \quad w = Ww', \quad t = Tt',$$

341 where $'$ denotes dimensionless quantities. By a similarity argument, we have that
 342 $W = \varepsilon U$.

343 Since the motors evolve on a smaller scale than the fluid, we introduce new char-
 344 acteristic scales. We take the microtubule half-length l as the length scale, the motor
 345 speed V_m as the velocity scale for motor evolution, and obtain a new time scale,
 346 $\tau = l/V_m$. We set

$$347 \quad s = ls', \quad V = V_m V', \quad t = \tau t'.$$

348 **2.3.1. Microtubule distribution.** To nondimensionalize Ψ we recall that it
 349 integrates to N , the number of microtubules. Furthermore, since the smooth delta
 350 function satisfies $\int \delta_a(z - z_0) dz = 1$, we define Ψ'_{z_0} as

$$351 \quad (33) \quad \Psi_{z_0}(\mathbf{x}_2, \theta, t) = \frac{N}{L^2} \Psi'_{z_0}(\mathbf{x}'_2, \theta, t')$$

352 so that $\iint \Psi'_{z_0} d\mathbf{x}'_2 d\theta = 1$. Alternatively, if we introduce the nondimensional smooth
 353 delta function $\delta'_{a'}(z' - z'_0)$ as $\delta_a(z - z_0) = \frac{1}{H} \delta'_{a'}(z' - z'_0)$ with $a' = a/H$ to mimic
 354 the behavior of a Dirac delta function, then we have for the full nondimensional
 355 density of microtubules $\Psi'(\mathbf{x}', \mathbf{p}, t') = \Psi'_{z_0}(\mathbf{x}'_2, \theta, t') \delta'_{a'}(z' - z'_0)$ and $\iiint \Psi' d\mathbf{x}' d\mathbf{p} = 1$.
 356 The microtubule evolution equation (19) is nondimensionalized on the same scale as
 357 the fluid equations. Therefore, plugging the definition of the rescaled quantities into
 358 Eqs. (19), (20) and (21) yields

$$359 \quad (34) \quad \partial_{t'} \Psi'_{z_0} + \nabla'_2 \cdot (\dot{\mathbf{x}}'_2 \Psi'_{z_0}) + \partial_\theta (\dot{\theta}' \Psi'_{z_0}) = 0$$

$$360 \quad (35) \quad \dot{\mathbf{x}}'_2 = -V'_{\text{sp}} \mathbf{p}_2 + \bar{\mathbf{u}}'_2 + A'_2 U'_{t,\parallel} \mathbf{p}_2 \mathbf{p}_2 : \nabla'_2 \mathbf{D}'_{2,z_0} - D'_{t,\parallel} \nabla'_2 \ln \Psi'_{z_0}$$

$$361 \quad (36) \quad \dot{\theta}' = (\nabla'_2 \bar{\mathbf{u}}'_2 + A'_2 U'_{r'} \mathbf{D}'_{2,z_0}) : \mathbf{p}_2 \mathbf{p}_2 - D'_r \partial_\theta \ln \Psi'_{z_0}$$

363 with constants $D'_{t,\parallel} = \frac{D_{t,\parallel} T}{L^2}$, $D'_r = D_r T$, $U'_{r'} = \frac{2U_r^0 NT}{HL^2}$, $U'_{t'} = \frac{U_{t,\parallel}^0 NT}{HL^4}$, $V'_{\text{sp}} = \frac{V_{\text{sp}}}{U}$,
 364 and $A'_2 = \int \delta_{a'}^2(z' - z'_0) dz' = HA_2$. We let $\tilde{U}'_{t,\parallel} = A'_2 U'_{t,\parallel}$ to simplify notation. The
 365 nondimensional form of the moment tensors are

$$366 \quad \mathbf{S}'_{z_0} = \frac{N}{L^2} \mathbf{S}_{z_0}, \quad \mathbf{D}'_{z_0} = \frac{N}{L^2} \mathbf{D}'_{z_0}.$$

367 **2.3.2. Motor distributions.** We nondimensionalize the bound motor distribu-
 368 tion \mathcal{M}_b so that it integrates to the ratio of bound to total motors:

$$369 \quad \iiint \mathcal{M}'_b \Psi' ds' d\mathbf{r}'_0 d\mathbf{x}' d\mathbf{p} = \frac{N_b}{N_m} \quad \text{and} \quad \iiint \mathcal{M}'_{b,z_0} \Psi'_{z_0} ds' d\mathbf{r}'_0 d\mathbf{x}'_2 d\theta = \frac{N_b}{N_m}.$$

370 Recalling that $\iiint \mathcal{M}_b \Psi ds d\mathbf{r}_0 d\mathbf{x} d\mathbf{p} = N_b$, plugging in the two-dimensional reduc-
 371 tions (17) and (22) and comparing to the above, we obtain

$$372 \quad (37) \quad \mathcal{M}_{b,z_0}(s, \mathbf{r}_0 | (\mathbf{x}_2, \theta), t) = \frac{N_m H}{l L^2 N A'_2} \mathcal{M}'_{b,z_0}(s', \mathbf{r}'_0 | (\mathbf{x}'_2, \theta), t^*)$$

373 and similarly for the full nondimensional distribution

$$374 \quad \mathcal{M}'_b(s, \mathbf{r}_0 | (\mathbf{x}, \mathbf{p}), t^*) = \frac{1}{A'_2} \mathcal{M}'_{b,z_0}(s, \mathbf{r}_0 | (\mathbf{x}_2, \theta), t^*) \delta'_{a'}(z' - z'_0).$$

375 We rescale the distribution of free motors to the fraction of free motors, setting $\mathcal{M}_f =$
 376 $\frac{N_m}{L^2} \mathcal{M}_f$ and $\mathcal{M} = \frac{N_m}{L^2} \mathcal{M}'$ to obtain

$$377 \quad (38) \quad \mathcal{M}'_f(\mathbf{r}'_0, t^*) = \mathcal{M}'(\mathbf{r}'_0) - \iiint \mathcal{M}'_{b,z_0} \Psi'_{z_0} ds' d\mathbf{x}'_2 d\theta.$$

378 Using these definitions and the second set of nondimensional variables, we have

$$379 \quad (39) \quad \begin{aligned} \partial_{t^*} \mathcal{M}'_{b,z_0} + \partial_{s'} \mathcal{M}'_{b,z_0} + \frac{\tau}{T} \dot{\mathbf{x}}'_2 \cdot \nabla_{2'} \mathcal{M}'_{b,z_0} - \frac{\tau}{T} \tilde{\zeta} \mathcal{M}'_{b,z_0} + \frac{\tau}{T} \dot{\theta}' \partial_\theta \mathcal{M}'_{b,z_0} \\ = -k'_{\text{off}} \mathcal{M}'_{b,z_0} + k'_{\text{on}} \mathcal{M}'_f \mathbb{1}_{D_{r'_c}}, \end{aligned}$$

380 together with the dimensionless fluxes

$$381 \quad \dot{\tilde{\mathbf{x}}}'_2 = -V'_{\text{sp}} \mathbf{p}_2 + \frac{1}{A'_2} \tilde{\mathbf{u}}'_2 + \frac{A'_3}{A'_2} U_{t,\parallel}^{0'} \mathbf{p}_2 \mathbf{p}_2 : \nabla'_2 \mathbf{D}'_{2,z_0} - D'_{t,\parallel} \nabla'_2 \ln \Psi'_{z_0}$$

$$382 \quad \dot{\tilde{\zeta}}' = \frac{1}{2A'_2} \widetilde{\partial_{z'} w'} - \frac{B'_1 U_{t,\perp}^{0'}}{A'_2} \mathbf{p}_2 \mathbf{p}_2 : \mathbf{D}'_{2,z_0}$$

$$383 \quad \dot{\tilde{\theta}} = \left(\frac{1}{A'_2} \nabla'_2 \tilde{\mathbf{u}}'_2 + \frac{A'_3}{A'_2} U_r^{0'} \mathbf{D}'_{2,z_0} \right) : \mathbf{p}_2^\perp \mathbf{p}_2 - D'_r \partial_\theta \ln \Psi'_{z_0}$$

384
385 and constants $A'_3 = H^2 A_3$, $U_{t,\perp}^0 = \frac{U_{t,\perp}^0 NT}{H^3 L^2}$, $B'_1 = H^4 B_1$, $k'_{\text{off}} = k_{\text{off}} \tau$, $k'_{\text{on}} =$
386 $k_{\text{on}} \tau \ln r_c / a$. We note that the dot in the above equations refers to a time deriva-
387 tive with respect to t^* . For completeness, we write the definition of the dimensionless
388 disk of radius r'_c centered at \mathbf{r}'_0 as

$$389 \quad D_{r'_c}(\mathbf{r}'_0) = \left\{ (\mathbf{x}'_2, s', \theta) : \left| \mathbf{x}'_2 + \frac{l}{L} s' \mathbf{p}_2 - \mathbf{r}'_0 \right|^2 \leq \frac{l^2}{L^2} r_c'^2 \right\}.$$

390 As the bound motor density timescale is approximately a thousand times smaller than
391 the microtubule timescale, we drop most of the terms with $\frac{\tau}{T}$ in Eq. (39), except the
392 terms involving the steric parameters $U_{t,\parallel}^{0'}$ and $U_r^{0'}$ as their product with τ/T could
393 end up being order one. We drop the term with $U_{t,\perp}^{0'}$, since our assumptions that
394 the motion of the microtubule is constrained to a plane makes it a small number.
395 Eliminating these terms we have

$$396 \quad (40) \quad \begin{aligned} \partial_{t^*} \mathcal{M}'_{b,z_0} + \partial_{s'} \mathcal{M}'_{b,z_0} + \frac{A'_3}{A'_2} \frac{\tau}{T} U_{t,\parallel}^{0'} \mathbf{p}_2 \mathbf{p}_2 : \nabla'_2 \mathbf{D}'_{2,z_0} \cdot \nabla'_2 \mathcal{M}'_{b,z_0} \\ + \frac{A'_3}{A'_2} \frac{\tau}{T} U_r^{0'} \mathbf{D}'_{2,z_0} : \mathbf{p}_2^\perp \mathbf{p}_2 \partial_\theta \mathcal{M}'_{b,z_0} = -k'_{\text{off}} \mathcal{M}'_{b,z_0} + k'_{\text{on}} \mathcal{M}'_f \mathbb{1}_{D_{r'_c}}. \end{aligned}$$

397 Again, for simplicity, we introduce $\widetilde{U}_{t,\parallel}^0 = A'_3 \tau U_{t,\parallel}^{0'} / (A'_2 T)$ and $\widetilde{U}_r^0 = A'_3 \tau U_r^{0'} / (A'_2 T)$.

398 For the simplified motor model, it is straightforward to see that the nondimen-
399 sional version of Eq. (27) is

$$400 \quad (41) \quad \mathcal{M}'_{b,z_0}(\mathbf{r}'_0, s' | (\mathbf{x}'_2, \theta), t^*) = \begin{cases} 0 & \text{if } (\mathbf{x}'_2, s', \theta) \notin D'_{r'_c} \\ \min \left(C', \frac{\mathcal{M}'(\mathbf{r}'_0)}{\iint_{D'_{r'_c}} \Psi'_{z'_0} d\mathbf{x}'_2 d\theta ds'} \right) & \text{if } (\mathbf{x}'_2, s', \theta) \in D'_{r'_c} \end{cases},$$

401 where C' is an independent problem specific parameter.

402 **2.3.3. Fluid.** To nondimensionalize the bulk fluid equations, we first rescale the
403 extra stresses as

$$404 \quad (42) \quad \boldsymbol{\sigma}^f = \sigma'_f \mathbf{S}'_{z_0}(\mathbf{x}_2, t) : \mathbf{E}'(\mathbf{x}, t) \delta'_a(z - z_0)$$

$$405 \quad (43) \quad \boldsymbol{\sigma}^t = -\sigma'_t (\mathbf{D}'_{z_0}(\mathbf{x}_2, t) \cdot \mathbf{D}'_{z_0}(\mathbf{x}_2, t) - \mathbf{S}'_{z_0}(\mathbf{x}_2, t) : \mathbf{D}'_{z_0}(\mathbf{x}_2, t)) \delta_a'^2(z - z_0),$$

407 and $\mathbf{E}(\mathbf{x}, t) = \frac{1}{T} \mathbf{E}'$, where \mathbf{E}' is dimensionless rate-of-strain tensor. Here, we note
408 that the dimensionless gradient of the velocity field has the form

$$409 \quad \nabla' \mathbf{u}'(\mathbf{x}, t) = \begin{pmatrix} \nabla'_2 \mathbf{u}'_2 & \frac{1}{\varepsilon} \partial_{z'} \mathbf{u}'_2 \\ \varepsilon (\nabla'_2 w')^T & \partial_{z'} w' \end{pmatrix}.$$

410 In Eqs. (42)-(43) the constants are $\sigma'_f = \frac{\sigma_f N}{T H L^2}$, and $\sigma'_t = \frac{\sigma_t N^2}{H^2 L^4}$. Plugging in Eq. (33)
 411 for Ψ and Eq. (37) for \mathcal{M}_b into the force density (15), changing variables and setting
 412 $F = F_{\text{st}} \left(1 - \frac{V_m}{V_{\text{max}}}\right) \frac{N_m}{L^2 H A_2^2}$, we obtain $\mathbf{f}_2(\mathbf{x}, t) = -F \mathbf{f}'_2(\mathbf{x}', t')$ where

$$413 \quad \mathbf{f}'_2(\mathbf{x}', t') = \delta_a'^2 (z' - z'_0) \iiint \mathbf{p}_2 \delta \left(\mathbf{y}'_2 + \frac{l}{L} s' \mathbf{p}_2 - \mathbf{x}'_2 \right) \Psi'_{z_0} \mathcal{M}'_{b, z_0} ds' dr'_0 dy'_2 d\theta.$$

415 Finally, we plug the nondimensional stresses and forces into the incompressible
 416 reduced Stokes equation (30)-(32) and we let the characteristic pressure be P_0 to find
 417 ($\varepsilon = H/L$)

$$418 \quad (44) \quad -\nabla_2'^2 \mathbf{u}'_2 - \frac{1}{\varepsilon^2} \partial_{z'_2} \mathbf{u}'_2 + P'_0 \nabla_2' q' = F' \mathbf{f}'_2 + \tilde{\sigma}_f \nabla_2' \cdot \boldsymbol{\sigma}^f - \tilde{\sigma}_t \nabla_2' \cdot \boldsymbol{\sigma}^t$$

$$419 \quad (45) \quad -\nabla_2'^2 w' - \frac{1}{\varepsilon^2} \partial_{z'_2} w' + P'_0 \partial_{z'_2} q' = 0$$

$$420 \quad (46) \quad \nabla_2' \cdot \mathbf{u}'_2 + \partial_{z'_2} w' = 0.$$

422 In the above, the constants are $P'_0 = \frac{P_0 L}{\mu U}$, $F' = \frac{F L^2}{\mu U}$, $\tilde{\sigma}_f = \frac{L}{\mu U} \sigma'_f$, and $\tilde{\sigma}_t = \frac{L}{\mu U} \sigma'_t$. In
 423 the remainder of this paper and the supplemental movies, we drop all prime, tilde
 424 and bar notation and numerically solve the complete set of nondimensional equations
 425 which are summarized in Table 1.

426 3. Implementation.

427 In this section, we discuss the discretization of the nondimensionalized equations
 428 summarized in Table 1 and the development of a stable algorithm. Because Ψ_{z_0} and
 429 \mathcal{M}_{b, z_0} evolve on two different timescales, we discretize Ψ_{z_0} at time t^n , $n = 0, \dots, N_T$
 430 with adaptive time step dt and \mathcal{M}_{b, z_0} at time t^m , $m = 0, \dots, N_{T^*}$ with smaller
 431 adaptive time step dt^* such that $t^n \leq t^m \leq t^{n+1}$. After initializing Ψ_{z_0} and \mathcal{M}_{b, z_0} ,
 432 we calculate the initial time step dt and, if the evolved motor model is being used, the
 433 initial time step dt^* as well. The motor forces and steric stresses are computed next,
 434 and used to solve the fluid equations. The new fluid velocities are used to update
 435 Ψ_{z_0} to time $t + dt$, and finally \mathcal{M}_{b, z_0} is updated to time $t + dt$ based on the updated
 436 Ψ_{z_0} . New time steps are computed, and the simulation continues. The procedure
 437 is summarized in Algorithm 1 and details are given below. Our numerical scheme
 438 is similar to that of our previous scheme in [11]. The primary differences are that
 439 the fluid equations are now solved in three dimensions, and that extra stress terms
 440 resulting from the steric interactions are included.

441 To compute the time step dt , we calculate the maximum of the angular and
 442 linear advection velocities in Eq. (33) and adjust the time step according to the CFL
 443 condition. To find the small time step for \mathcal{M}_b , we limit the fraction of available
 444 motors that can bind or unbind in any given time step. To calculate dt^* , we compare
 445 the change due to s -advection with the greatest change due to binding and unbinding,
 446 and use the more restrictive of the two to clamp dt^* .

447 **3.1. Microtubule density.** We discretize $\Psi_{z_0}(\mathbf{x}_2, \theta)$ over the domain $(\mathbf{x}_2, \theta) \in$
 448 $[-1, 1]^2 \times [0, 2\pi]$ at the plane of motion $z = z_0$ with a triply periodic grid of size
 449 $N_x \times N_y \times N_\theta$, with $N_x = N_y$. The advection terms in (MT1) (Table 1) are discretized
 450 spatially with an upwinding scheme and Superbee flux limiter [6]. The equation (MT1)
 451 is integrated in time using second order Adams-Bashforth for the advective terms and
 452 Crank-Nicolson for the diffusive terms. The resulting system of equations for Ψ_{z_0} is
 453 solved using the Conjugate Gradient method with Incomplete Cholesky factorization
 454 used as a preconditioner.

Model Summary

Microtubules

$$\partial_t \Psi_{z_0} + \nabla_2 \cdot (\dot{\mathbf{x}}_2 \Psi_{z_0}) + \partial_\theta (\dot{\theta} \Psi_{z_0}) = 0 \quad (\text{MT1})$$

$$\dot{\mathbf{x}}_2 = -V_{\text{sp}} \mathbf{p}_2 + \mathbf{u}_2 + U_{t,\parallel}^0 \mathbf{p}_2 \mathbf{p}_2 : \nabla_2 \mathbf{D}_{2,z_0} - D_{t,\parallel} \nabla_2 \ln \Psi_{z_0} \quad (\text{MT2})$$

$$\dot{\theta} = (\nabla_2 \mathbf{u}_2 + U_r^0 \mathbf{D}_{2,z_0} : \mathbf{p}_2^\perp \mathbf{p}_2 - D_r \partial_\theta \ln \Psi_{z_0}) \quad (\text{MT1})$$

Motors

$$\begin{aligned} \partial_t \mathcal{M}_{b,z_0} + \partial_s \mathcal{M}_{b,z_0} + U_{t,\parallel}^0 \mathbf{p}_2 \mathbf{p}_2 : \nabla_2 \mathbf{D}_{2,z_0} \cdot \nabla_2 \mathcal{M}_{b,z_0} \\ + U_r^0 \mathbf{D}_{2,z_0} : \mathbf{p}_2^\perp \mathbf{p}_2 \partial_\theta \mathcal{M}_{b,z_0} = -k_{\text{off}} \mathcal{M}_{b,z_0} + k_{\text{on}} \mathcal{M}_f \mathbb{1}_{D_{r_c}} \end{aligned} \quad (\text{EM})$$

$$\mathcal{M}_{b,z_0} = \begin{cases} 0 & \text{if } |\mathbf{x}_2 + \frac{l}{L} s \mathbf{p}_2 - \mathbf{r}_0| \geq r_c \\ \min \left(C, \frac{\mathcal{M}(\mathbf{r}_0)}{\iint_{D_{r_c}} \Psi_{z_0} d\mathbf{x}_2 d\mathbf{p}_2 ds} \right) & \text{if } |\mathbf{x}_2 + \frac{l}{L} s \mathbf{p}_2 - \mathbf{r}_0| < r_c \end{cases} \quad (\text{SM})$$

$$\mathcal{M}_f = \mathcal{M} - \iiint \mathcal{M}_b \Psi_{z_0} ds d\mathbf{x}_2 d\theta \quad (\text{MF})$$

Fluid

$$-\nabla_2^2 \mathbf{u}_2 - \frac{1}{\varepsilon^2} \partial_{zz} \mathbf{u}_2 + P_0 \nabla_2 q = \sigma_f \nabla_2 \cdot \boldsymbol{\sigma}^f - \sigma_t \nabla_2 \cdot \boldsymbol{\sigma}^t + F \mathbf{f}_2 \quad (\text{U1})$$

$$-\nabla_2^2 w - \frac{1}{\varepsilon^2} \partial_{zz} w + P_0 \partial_z q = 0 \quad (\text{U2})$$

$$\nabla_2 \cdot \mathbf{u}_2 + \partial_z w = 0 \quad (\text{U3})$$

Force

$$\mathbf{f}_2 = F \delta_a^2 (z - z_0) \iiint \mathbf{p}_2 \delta(\mathbf{y}_2 + \frac{l}{L} s \mathbf{p}_2 - \mathbf{x}_2) \Psi_{z_0} \mathcal{M}_{b,z_0} ds d\mathbf{r}_0 d\mathbf{y}_2 d\theta \quad (\text{F1})$$

Table 1: Summary of the nondimensionalized model equations for the evolution of microtubules, motors and fluid in a gliding assay. The primes and nondimensionalizing constants have been dropped for simplicity.

455 **3.2. Motor distributions.** To advance \mathcal{M}_{b,z_0} forward in time according to
 456 the evolved motor model (EM) in Table 1, two-step Adams-Bashforth with variable
 457 timestep dt^* is used to discretize the s-advection term and the binding and unbinding
 458 terms. We clamp $\mathcal{M}_{b,z_0}(\mathbf{r}_0, s|\mathbf{x}_2, \theta)$ so that $\iiint \mathcal{M}_{b,z_0} \Psi_{z_0} ds d\mathbf{x}_2 d\theta \leq \mathcal{M}(\mathbf{r}_0)$.

459 The bound motor density \mathcal{M}_{b,z_0} is high-dimensional as it tracks motor tail posi-
 460 tion, the filament arclength parameter, and the center of mass and orientation of the
 461 filament the bound motor head is attached to. However, since a head detaches if the
 462 elongation of the motor stalk exceeds a certain threshold, \mathcal{M}_{b,z_0} can be computed and
 463 stored sparsely in a local grid around \mathbf{r}_0 . The specific condition $\mathbf{x}_2 + \frac{l}{L} s \mathbf{p}_2 - \mathbf{r}_0 \leq r_c$
 464 allows further pruning of this localized configuration space. In our formulation, the
 465 activity of the motors anchored at \mathbf{r}_0 is independent of motors anchored elsewhere. In
 466 discrete form each cell \mathbf{y} stores the local grid over \mathbf{x}, θ, s for bound motors whose tails
 467 are anchored anywhere within the boundaries of cell \mathbf{y} . Each cell's motor distribution
 468 is updated in parallel. \mathcal{M}_{b,z_0} is stored as a two-dimensional array over \mathbf{r}_0 , each con-

Algorithm 1 Numerical evolution scheme for the coupled microtubule density, motor protein distribution, and fluid velocity equations.

```

Initialize  $\Psi_{z_0}$  and  $\mathcal{M}_{b,z_0}$ .
Precompute  $LU$ -decomposition of semi-spectral matrices for all frequency pairs.
while  $t < t_{\text{end}}$  do
  Compute adaptive  $dt$ .
  Compute  $\Psi_{z_0}(t+dt)$  by solving (MT1)-(MT3) using second order Crank-Nicolson
  for the diffusive terms and Adams-Bashforth 2 for the advection terms.
  if (using EM) then
    set  $t_{\text{end}}^* = t + dt$ .
    while  $t^* < t_{\text{end}}^*$  do
      Compute adaptive  $dt^*$ .
      Compute  $\mathcal{M}_{b,z_0}(t^* + dt^*)$  by solving (EM) with Adams-Bashforth 2.
      Update  $\mathcal{M}_f$  from  $M_{b,z_0}$  with (MF).
    end while
  else if (using simplified motor model) then
    Solve (SM)
    Update  $\mathcal{M}_f$  from  $M_{b,z_0}$  with (MF).
  end if
  Calculate extra stresses.
  Calculate motor force (F1) using trapezoidal rule and a local grid.
  Solve semi-spectral (U1)-(U3).
end while

```

469 taining an unrolled flat array for \mathbf{x}_2, s, θ . We solve the evolved motor density equation
470 on the GPU, where each \mathbf{r}_0 is updated in SIMD fashion by several threads. Another
471 advantage to this layout is that \mathcal{M}_{b,z_0} independent outermost two-dimensional array
472 can be split up and sent to multiple GPUs, or solved in batches on a single GPU if the
473 shared memory is exceeded. As grid resolution increases, the three copies of \mathcal{M}_{b,z_0} at
474 the current and two previous times required by the two-step Adams-Bashforth time
475 integration scheme may not all fit onto the GPU on-board memory simultaneously
476 and instead need to be solved a few rows at a time.

477 Since we do not track free motor heads, we can discretize the distribution of free
478 motors \mathcal{M}_f and total motors \mathcal{M} over a uniform grid of size $N_x \times N_y$. Updating \mathcal{M}_f
479 from \mathcal{M} and \mathcal{M}_{b,z_0} is straightforward and parallelizable over \mathbf{x}_2 by evaluating the
480 discretized form of (MF) in Table 1.

481 **3.3. Fluid.** We discretize the domain into $N_x \times N_y \times N_z$ grid cells, where $N_x =$
482 N_y , and solve for the fluid state at each discrete time t^n . \mathbf{u}_2 and q are sampled at cell
483 centers, while w is sampled at the z faces. As we have periodic boundary conditions
484 in the \mathbf{x}_2 -plane, we use a semi-spectral approach and take the Fourier transform in
485 \mathbf{x}_2 of (U1)-(U3), giving for each frequency pair $\mathbf{k} = (k_x k_y)^T$

$$486 \quad (47) \quad (|\mathbf{k}|^2 - \frac{1}{\varepsilon^2} \partial_{zz}) \hat{\mathbf{u}}_2^n + iP_0 \hat{q}^n \mathbf{k} = F \hat{\mathbf{f}}_2^n + i\sigma_f \hat{\sigma}^t{}^n \mathbf{k} + i\sigma_t \hat{\sigma}^t{}^n \mathbf{k}$$

$$487 \quad (48) \quad (|\mathbf{k}|^2 - \frac{1}{\varepsilon^2} \partial_{zz}) \hat{w}^n + P_0 \partial_z \hat{q}^n = 0$$

$$488 \quad (49) \quad i\mathbf{k} \cdot \hat{\mathbf{u}}_2^n + \partial_z \hat{w}^n = 0.$$

Equations (47)-(49) yield an independent $(4N_z - 1) \times (4N_z - 1)$ linear system for each frequency pair. This formulation is computationally advantageous for several reasons. First, the equations for each \mathbf{k} can be solved independently, allowing simple parallelization. Second, the coefficient matrix of each linear system is constant in time, and an LU-factorization for each can be precomputed and stored. We can reasonably store $N_x \times \frac{N_y}{2}$ separate $(4N_z - 1) \times (4N_z - 1)$ matrices, and use them to solve for multiple right-hand sides. The FFTW library [8] is used with precomputed transformation mappings to efficiently perform the FFT and inverse FFT.

As the microtubules are concentrated around the $z = z_0$ plane, it is desirable to have more accuracy there and the thin δ_a -width region around it than in the distant assay regions above and below it. Given the aforementioned scaling of each frequency pair fluid solve matrix with N_z^2 , we use a nonuniform grid with variable spacing in the z dimension. We store $\hat{\mathbf{u}}_2$, and \hat{q} at the z -cell centers, and \hat{w} at the z -cell faces. A schematic of the z -grid is shown in Figure 3.

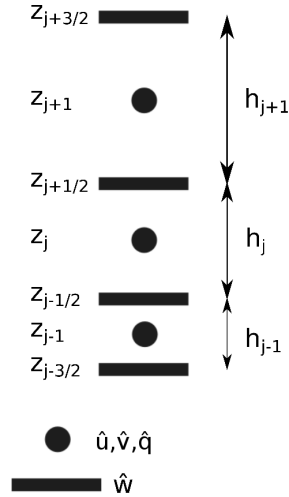


Fig. 3: Schematic of the nonuniform staggered grid in z used to store the spectral values of $\hat{\mathbf{u}}, \hat{w}, \hat{p}$.

503

504

To compute second derivatives with respect to z at a z -cell j , we construct a fourth order Lagrange interpolating polynomial using $z_{j-2}, z_{j-1}, z_j, z_{j+1}, z_{j+2}$, and differentiate twice. Near the boundaries, we use boundary data and the no slip boundary condition for the extreme samples and drop to third order interpolation for the bottom-most and top-most equations. For first derivatives at a z -face $j + 1/2$, we construct a third order Lagrange interpolating polynomial using $z_{j-1}, z_j, z_{j+1}, z_{j+2}$, and differentiate once. Near the boundaries, we use the nearest four samples to construct the interpolating polynomial.

512

The motor force calculation is the single most computationally intense portion of the algorithm because the force spreading dictates that nearby forces be calculated in order to determine the total force at \mathbf{x} . In terms of implementation, this effectively increases the already high dimensionality of the bound motor distribution, whether it is approximated with the simple motor model or the evolved motor model. To account for the motor force's highly parallel but computationally intensive nature, it is calculated on a GPU using a similar scheme to the bound motor solve described above.

518

519 A speedup of roughly forty times is observed versus a single-core implementation.

520 Computation of the stress tensors is straightforward and parallelizable. σ^f
 521 depends on the rate-of-strain tensor \mathbf{E} , which we have only for the previous time step
 522 since we compute the extra stresses before the fluid solve. We therefore linearly ex-
 523 trapolate \mathbf{E} at the new time $t + dt$ using the current and previous values, as in [7].

524 **4. Results.** In this section, we present results for various experiments with the
 525 following parameters held constant: $2\mu\text{m}$ -length microtubules, $k_{\text{on}} = 25$, $k_{\text{off}} = .1$,
 526 $U_t = -.01$, $125 \times 125 \mu\text{m}^2$ assay, $N_m = 3 \times 10^6$ motors, $V_{\text{max}} = 1 \mu\text{ms}^{-1}$, and $N = 22300$
 527 microtubules. Our nonuniform z -grid has 30 evenly sized fine z -cells covering the range
 528 $\{-.5, -.4\}$, with $z_0 = \frac{-h}{2} + .05 = -.45$ in the middle. Above $z = -.4$, the height of
 529 each cell doubles consecutively until the cell size is sixteen times greater than the fine
 530 z -cells at the bottom. Our final 3D grid dimensions are $128 \times 128 \times 49$, with 32 cells
 531 in s and θ .

532 In the figures, we plot the nondimensionalized spatial microtubule distribution

$$533 \quad (50) \quad \Psi_{\text{spatial}, z_0}(\mathbf{x}_2, t) = \int \Psi_{z_0}(\mathbf{x}_2, \theta, t) d\theta$$

534 with color ranging from white (low) to blue (high). We plot the nondimensional
 535 spatial bound motor distribution

$$536 \quad (51) \quad \mathcal{M}_{\text{b,spatial}, z_0}(\mathbf{r}_0, t) = \iiint \mathcal{M}_{\text{b}, z_0}(s, \mathbf{r}_0, t | \mathbf{x}_2, \theta) \Psi_{z_0}(\mathbf{x}_2, \theta, t) ds d\mathbf{x}_2 d\theta$$

537 with color ranging from tan (low) to red (high). The colorbars are annotated with the
 538 corresponding percentage of the total available motors in the bound configuration, at
 539 the low and high ranges of each normalization. Finally, we compute the orientation
 540 matrix

$$541 \quad (52) \quad \mathbf{N}(\mathbf{x}_2, t) = \frac{\int \mathbf{p}_2 \mathbf{p}_2^T \Psi_{z_0}(\mathbf{x}_2, \theta, t) d\theta}{\int \Psi_{z_0}(\mathbf{x}_2, \theta, t) d\theta}$$

542 and draw its eigenvectors in red scaled by their associated eigenvalues. When present,
 543 velocity vectors (black) and orientation eigenvectors are plotted for every fifth cell for
 544 clarity.

545 4.1. Evolved motor model.

546 *Single clump.* We first examine the processive behavior of a clump of aligned filaments
 547 as the steric alignment parameter is varied between $U_r = 0$ and $.01$. We present
 548 results for $U_r = 0, .01$ and the evolved motor model in Figure 4. We observe that
 549 as U_r increases to $.01$ the clump better maintains its shape, whereas at $U_r = 0$
 550 microtubules become concentrated along the leading edge of the clump, which assumes
 551 a widening crescent-like shape. The bottom row of Figure 5 shows the microtubule
 552 orientation field at the final frame displayed in the upper rows with $U_r = 0$ (left)
 553 and $U_r = .01$ (right). For higher values of U_r , the microtubule orientation field is
 554 uniformly aligned. For smaller values of U_r , the microtubule orientation field at the
 555 clump's leading edge becomes tangential to the leading edge, as the rods rotate to
 556 avoid compression or extension by the steep velocity gradient, clearly visible in the
 557 $U_r = 0$ case. For $U_r = .01$, the steric resistance to rotate relative to neighboring
 558 microtubules counteracts this effect and the orientation field remains more uniform.
 559 *In vitro* experiments have shown shape persistence in aligned clumps [28], qualitatively
 560 similar to the $U_r = .01$ case.

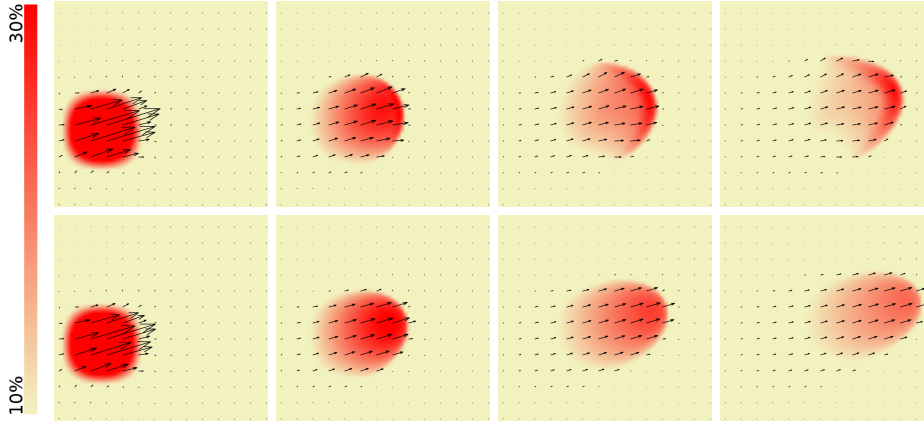


Fig. 4: Single aligned microtubule clump driven by the evolved motor model. First row: $U_r = 0$ velocity field. Second row: $U_r = .01$ velocity field. Images are at times $t=0, 15, 30,$ and 45 sec.

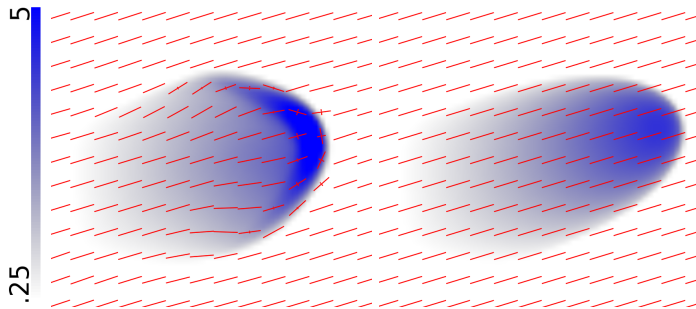


Fig. 5: Single aligned clump orientation field at time $t=45$ sec for $U_r = 0$ (left) and $U_r = .01$ (right).

561 *Colliding clumps.* We examined the behavior of colliding clumps for three values of
 562 the steric alignment parameter $U_r = 0, .001, .01$ and both head-on and perpendicular
 563 collisions. When clumps collide, the behavior depends on the angle between the
 564 microtubule orientations of the clumps.

565 A nearly perpendicular collision as in Figure 6 results in the clumps merging and
 566 moving as a single clump for all U_r tested. While the U_r term drives local alignment,
 567 alignment also occurs in the $U_r = 0$ case as follows. When the self-propulsion velocity
 568 is zero, microtubules move passively with the flow. As motor forces act directly on
 569 the fluid, motor forces acting in opposite directions cancel out. This cancellation
 570 occurs in the example depicted in Figure 6, where the resultant force points in the
 571 average direction of the colliding microtubule orientations, in this case, upwards.
 572 These two mechanisms give different qualitative results as illustrated in Figure 6. In
 573 the $U_r = 0$ case (third row), the microtubule distribution remains isotropic as long as
 574 local fluid flow remains negligible, whereas in the $U_r = .01$ case (fourth row), we
 575 observe steric alignment of the microtubules throughout the entire domain. Higher U_r

576 results in steeper gradients in microtubule orientation and density at the midline. The
 577 higher concentration in turn leads to stronger motor forces and higher fluid velocities.
 578 These U_r -dependent collision phenomena are observed wherever two regions of dense
 microtubules collide.

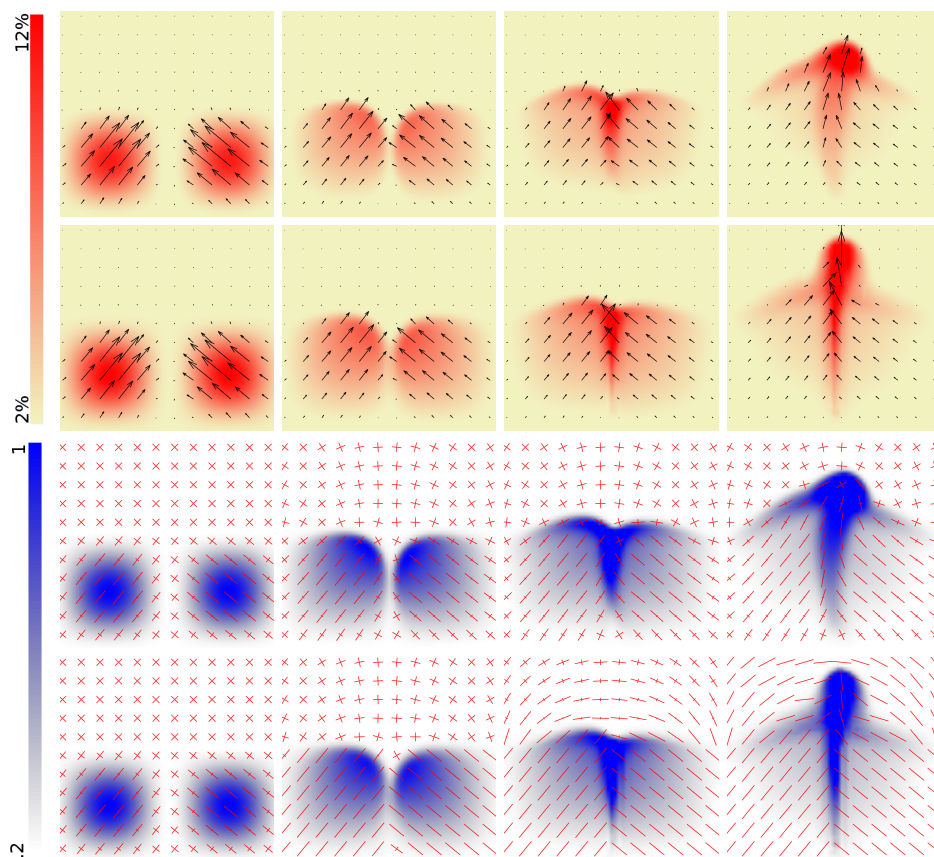


Fig. 6: Nearly perpendicular microtubule clumps driven by the evolved motor model colliding. First row: $U_r = 0$ velocity field. Second row: $U_r = .01$ velocity field. Third row: $U_r = 0$ orientation field. Fourth row: $U_r = .01$ orientation field. Images are at times $t=0, 45, 90,$ and 180 sec.

579

580 In the case of two clumps with antiparallel orientations colliding close to head-on
 581 (Figure 7, supplemental movie 1 first example), significant differences are observed
 582 for $U_r = 0$ versus $U_r = .01$. In the $U_r = 0$ case, the motor forces drive an extensional
 583 fluid flow on either side of the collision centerline, creating two clumps moving in
 584 opposite directions. In the case $U_r = .01$, the steric force prevents alignment with
 585 the extensional flow and the microtubules of each clump slide past each other. As
 586 a result of slight differences in the original clump position, the clumps break down
 587 after collision, and smaller clumps pass through each other and continue along the
 588 initial clump trajectories. The orientation field (Figure 7, fourth row) shows that the
 589 microtubules do not rotate during the initial collision and aftermath.

590 *Vortex Lattice.* To test our model's ability to reproduce characteristics of the

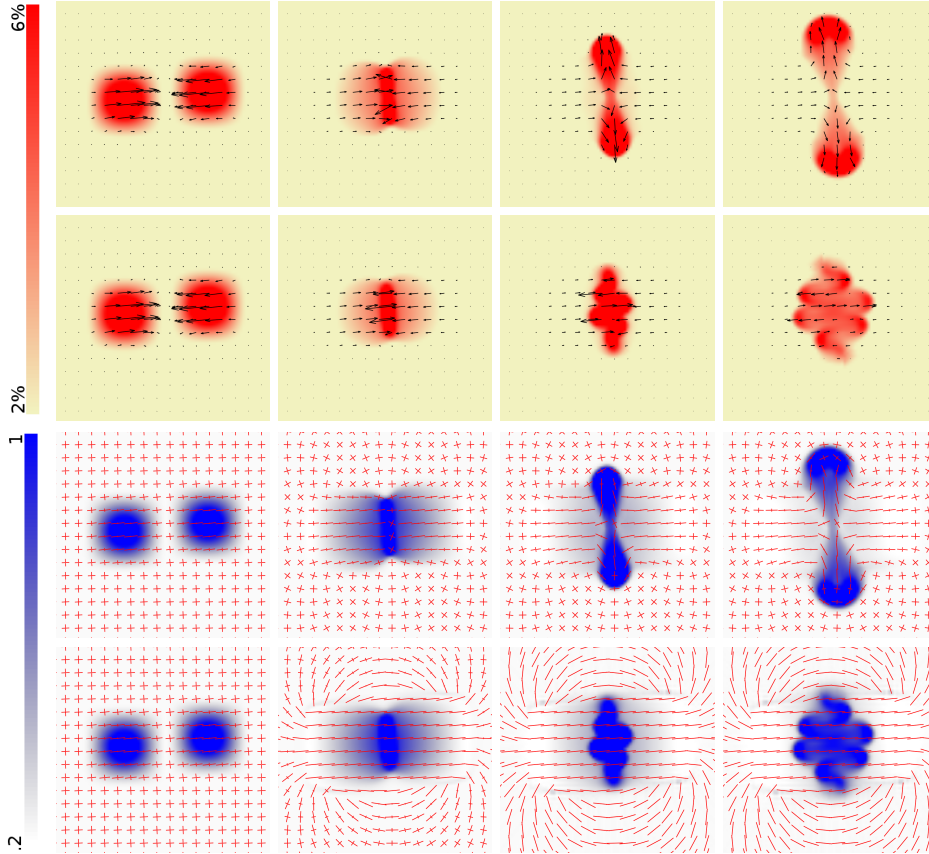


Fig. 7: Antiparallel microtubule clumps driven by the evolved motor model colliding. First row: $U_r = 0$ velocity field. Second row: $U_r = .01$ velocity field. Third row: $U_r = 0$ orientation field. Fourth row: $U_r = .01$ orientation field. Images are at times $t=0, 90, 180,$ and 270 sec. See supplemental movie 1 first example.

591 lattice of vortices observed in [32], we simulate four overlapping rings of microtubules
 592 oriented in clockwise fashion as shown in Figure 8 and the first example in supple-
 593 mental movie 2. In the overlapping regions, the microtubules from adjacent rings are
 594 oriented opposite each other. We observe extensional flow in the dense overlapping
 595 regions combined with counterclockwise rotation driven by the initial orientations.
 596 With $U_r = 0$ the rotational flow develops four vortices rotating clockwise centered
 597 about the spaces between the initial four vortices. The new vortices contract then
 598 expand outward until they develop overlapping regions moving in opposite directions,
 599 similar to the initial condition. The process repeats itself; extensional flow and rota-
 600 tion forms again in the overlapping regions, leading to the formation of four vortices
 601 rotating counterclockwise at the original four vortex locations. Due to diffusion, the
 602 maximum concentration and hence velocity decreases on average throughout the pro-
 603 cess. Due to symmetry breaking, the transition from vortices with overlapping regions
 604 to new vortices with overlapping regions and opposite rotation repeats a few times
 605 at most, depending on parameters, until the original structure is lost. Increasing U_r

606 from 0 to .01 increases the maximum microtubule density and flow velocity and gives
 607 steeper gradients in microtubule concentration and orientation, as seen in previous
 608 examples. It also affects the degree to which the initial dense overlapping regions
 609 break down with the rotational forcing from the motor proteins. In particular, for
 610 $U_r = .01$ (Figure 8, second and fourth rows), the dense overlapping regions extend but
 611 do not separate and thus preserve much of the original four vortex structure. With
 612 the inclusion of the steric interaction term, our results are more consistent with the
 613 experiments of [32], which demonstrate a temporally persistent lattice of vortices.

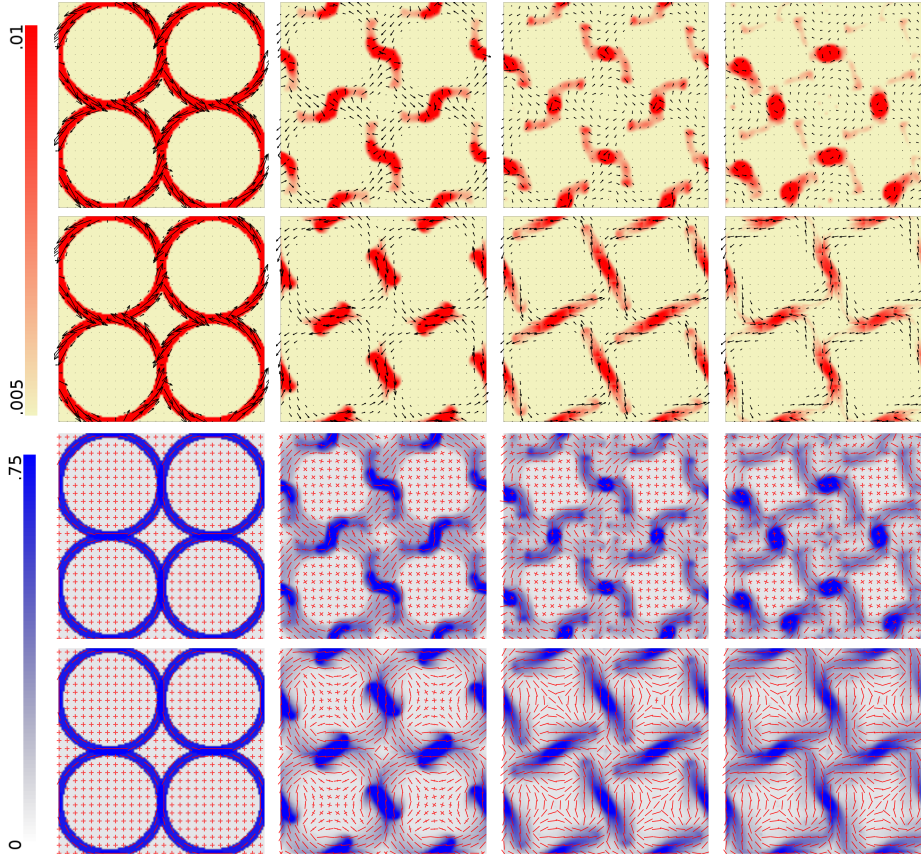


Fig. 8: Vortex lattice experiment with evolved motor model. First row: $U_r = 0$ velocity field. Second row: $U_r = .01$ velocity field. Third row: $U_r = 0$ orientation field. Fourth row: $U_r = .01$ orientation field. Images are at times $t=0, 240, 480,$ and 720 sec. See supplemental movie 2 first example.

614 *Perturbation.* We perturb a uniform isotropic microtubule density in both space
 615 and orientation by adding

$$616 \quad (53) \quad \frac{1}{a} \sum_{i,j=1}^8 \epsilon_{ij} \cos(\pi i x + \xi_{ij}) \cos(\pi j y + \xi_{ij}) P_{ij}(\theta),$$

617
 618 where ϵ_{ij} is a uniform random number in $[-.001, .001]$, ξ_{ij} is a uniform random number
 619 in $[0, 2\pi]$, a is a normalization constant and $P_{ij}(\theta)$ are third order polynomials in

620 $\cos(\theta)$ and $\sin(\theta)$ with random coefficients in $[-1, 1]$. The $U_r = 0$ case results in a
 621 spatiotemporally stable Ψ_{z_0} density (Figure 9, supplemental movie 3). In the $U_r = .01$
 case, continuous narrow tracks of stationary microtubules form and remain stable.

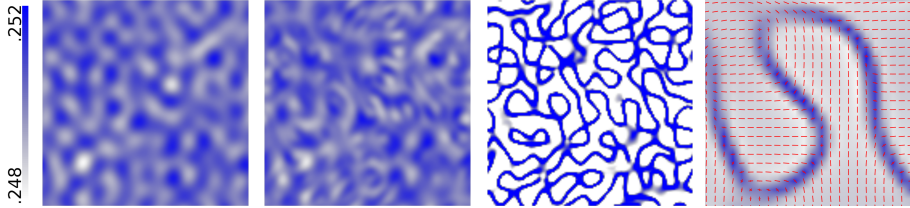


Fig. 9: Perturbation in x and θ giving rise to stationary concentrated pattern with $U_r = .01$ for evolved motor model. First three images: evolution of microtubule density in time. Fourth image: magnified section of final top row image with orientation eigenvectors in red. The microtubule density concentrates along steep gradients in the microtubule orientation field. Images are at times $t=0, 75,$ and 113 sec. See supplemental movie 3.

622

623 4.2. Evolved motor model with self-propulsion.

624 *Colliding clumps.* We repeat the antiparallel colliding clumps experiment with the
 625 addition of a self-propulsion velocity V_{sp} (Eq. (2), (MT2)) in Figure 10 and the second
 626 two examples in supplemental movie 1. In the case of $V_{sp} = 0$, illustrated in Figure 7,
 627 the clumps break up as they collide. At $V_{sp} = 1$ and $U_r = .01$, the clumps pass through
 628 each other largely intact. For $V_{sp} = 1$ and $U_r = 0$, we see a combination of both effects,
 629 with some passthrough and some spreading of microtubules with the extensional flow
 630 formed in the collision. In general, varying the value of V_{sp} between 0 and 1 leads
 631 to a corresponding combination of the extreme $V_{sp} = 0$ and $V_{sp} = 1$ behaviors. The
 632 experiments of [28] demonstrate a combination of passthrough and breakup when
 633 clumps collide. Experiments of the behaviors of microtubules undergoing collisions
 634 [32] show that colliding microtubules can merge and realign or pass through depending
 635 on the angle of collision. With the addition of a self-propulsion term, our numerical
 636 experiments reproduce such behaviors.

637 *Vortex rings.* We repeat the four ring vortex experiment with the addition of a
 638 self-propulsion velocity V_{sp} (Figure 11, second and third examples in supplemental
 639 movie 2). With $V_{sp} = .1$ and $U_r = 0$, depicted in the first row, motor forces at the
 640 overlapping regions of the initial rings create a shear flow that separates these regions
 641 and, in conjunction with the self-propulsion, creates counterclockwise vortices at the
 642 separatrix between clockwise vortices as seen in the second image of the first row. This
 643 separates the dense bands of microtubules into two connected bands that translate
 644 and rotate away from each other, eventually meeting other bands at the centers of the
 645 original rings in a cross-like pattern (third image). The microtubules gather at the
 646 centers of the crosses, then reverse direction and expand outward in a nonsymmetric
 647 way (fourth image), similar to the switching behaviors observed when the experiment
 648 is run without self-propulsion (Figure 8). With $V_{sp} = .1$ and $U_r = .01$, depicted in the
 649 second row, the steric alignment prevents the shear flow from separating the initial
 650 overlapping regions, and the self-propulsion drives antiparallel sliding that stretches
 651 the dense microtubule regions into long cohesive bands (second image, second row).
 652 The bands break down into smaller clumps (third image), but the steric alignment

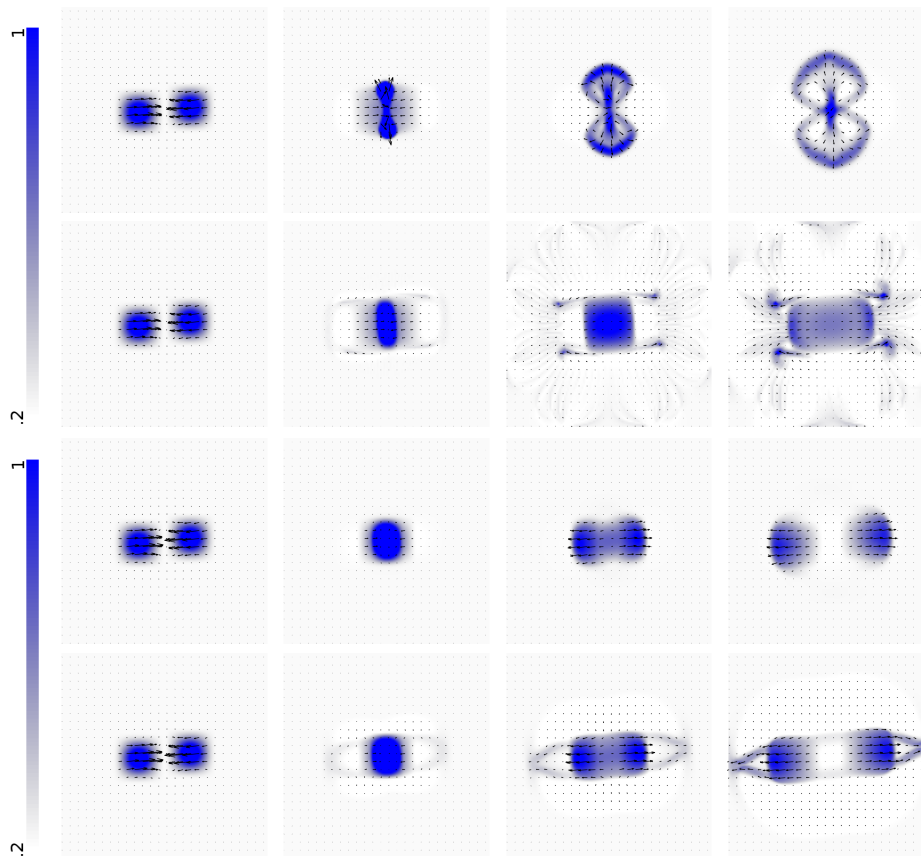


Fig. 10: Colliding clump experiment with added self-propulsion velocity. First row: $U_r = 0$ and $V_{sp} = .1$. Second row: $U_r = .01$ and $V_{sp} = .1$. Third row: $U_r = 0$ and $V_{sp} = 1$. Fourth row: $U_r = .01$ and $V_{sp} = 1$. Images are at times $t=0, 105, 210, 315$ sec in rows one and two, and at $t=0, 24, 48, 72$ sec in rows three and four. See second and third examples in supplemental movie 1.

653 term keeps the new clumps following the paths of the initial bands, which roughly
 654 correspond with the initial four vortex structure (fourth image) as observed without
 655 self-propulsion (Figure 8). Increasing the self-propulsion velocity to $V_{sp} = 1$ causes the
 656 self-propulsion to dominate the effects of the motor forces, so microtubule passthrough
 657 (with alignment if $U_r > 0$) becomes dominant. With $U_r = 0$ (third row), switching
 658 events occur continuously and the four quadrants of the assay are symmetric. We
 659 observe that with $U_r = .01$, passthrough rapidly breaks up the ring structure (fourth
 660 row). As a result, no switching events occur.

661 *Perturbation* We repeat the perturbation experiment with the addition of a self-
 662 propulsion velocity V_{sp} (Figure 12, second and third examples in supplemental movie
 663 3). At $V_{sp} = 1$ or $.1$ and $U_r = 0$ the clumps translate but simply pass through
 664 one another without increasing in density or aligning. With $V_{sp} = .1$ and $U_r = .01$
 665 (first row), we get fast translational microtubule bands as opposed to the stationary
 666 continuous tracks in the $V_{sp} = 0$ case shown in Figure 9. At $V_{sp} = 1$ and $U_r = .01$

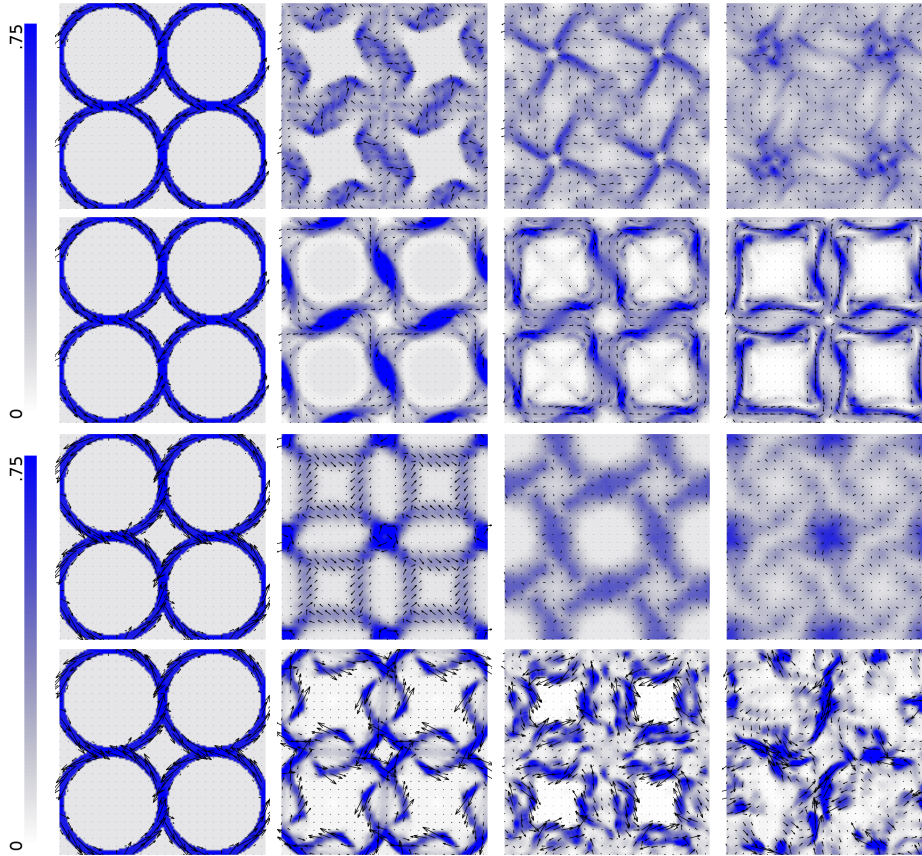


Fig. 11: Vortex ring experiment with added self-propulsion velocity. Images are illustrative of behavior and thus are not necessarily taken at the same simulation time between rows. First row: $U_r = 0$ and $V_{sp} = .1$. Second row: $U_r = .01$ and $V_{sp} = .1$. Third row: $U_r = 0$ and $V_{sp} = 1$. Fourth row: $U_r = .01$ and $V_{sp} = 1$. Images are at times $t=0, 225, 450, 675$ sec in rows one and two, and at $t=0, 60, 120, 180$ sec in rows three and four. See second and third examples in supplemental movie 2.

667 (second row), the bands form faster and are denser than in the $V_{sp} = .1$ case.

668 4.3. Simplified motor model.

669 *Vortex rings.* For the parameters, experiments, and timescales presented here, the
 670 differences in density and feature shape and location are observed between the mi-
 671 crotubule distribution fields generated by the simplified and evolved motor models
 672 are minor. One notable exception is that in the vortex ring experiment, the evolved
 673 motor model drives clockwise rotation in the four central clumps whereas the sim-
 674 plified motor model drives counterclockwise rotation (Figure 13). This effect is due
 675 to a slight difference in the motor force pattern around each clump. On timescales
 676 longer than those presented in this work, simulations may eventually show significant
 677 divergence.

678 *Colliding clumps.* Results from the antiparallel colliding clump simulation driven
 679 by the simplified motor model are presented in Figure 14 (supplemental movie 4)

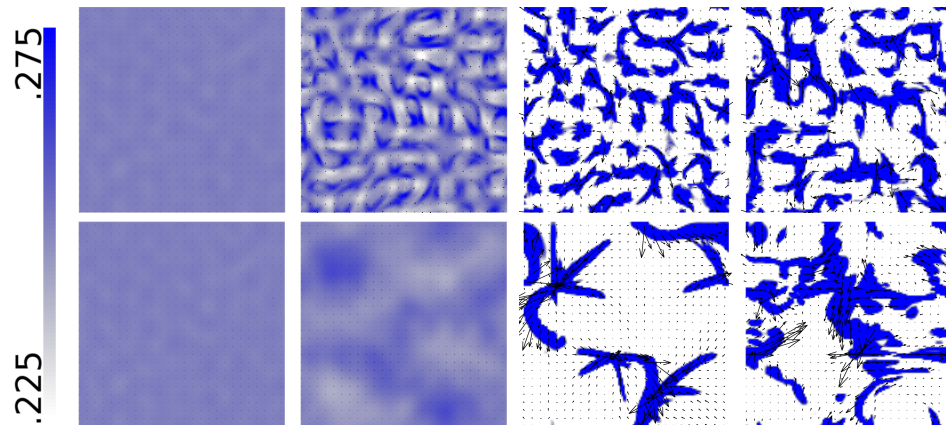


Fig. 12: Perturbation experiment with added self-propulsion velocity. First row: $U_r = .01$ and $V_{sp} = .1$. Second row: $U_r = .01$ and $V_{sp} = 1$. Images are at times $t=0, 105, 210, 315$ sec. See second and third examples in supplemental movie 3.

680 for values of the parameter $C = 10, 50, 250$. Increasing C not only increases the
 681 fluid velocities in the simulation by increasing value of $\mathcal{M}_{b,spatial,z_0}$ for a given Ψ_{z_0} ,
 682 but also changes the flow features that emerge over time. We observe that for the
 683 highest tested value $C = 250$, any cell with a $\Psi_{spatial,z_0}$ value over a threshold results
 684 in fully bound motors, exercising the second argument to the minimum function in
 685 the definition of the simplified motor model (SM). Therefore two cells with distinct
 686 $\Psi_{spatial,z_0}$ values above the threshold will produce motor forces of equal magnitude,
 687 changing the emergent behavior within the assay.

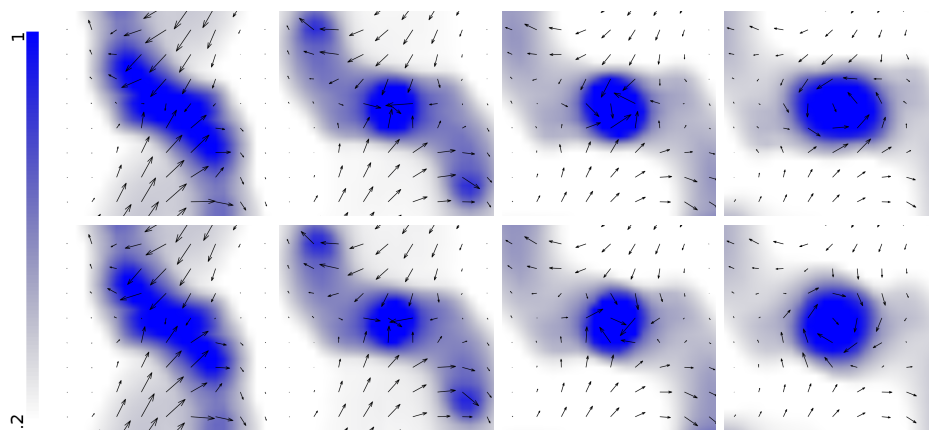


Fig. 13: Magnified view of vortex ring experiment with evolved motor model (top row) and simplified motor model (bottom row), $U_r = 0$ and $V_{sp} = 0$. A counter-clockwise velocity field forms with the evolved motor model, whereas a clockwise velocity field forms with the simplified motor model. Images are at times $t=150, 300, 450, 600$ sec.

688 *Perturbation with and without motor-based fluid forces.* In Figure 15 (supple-

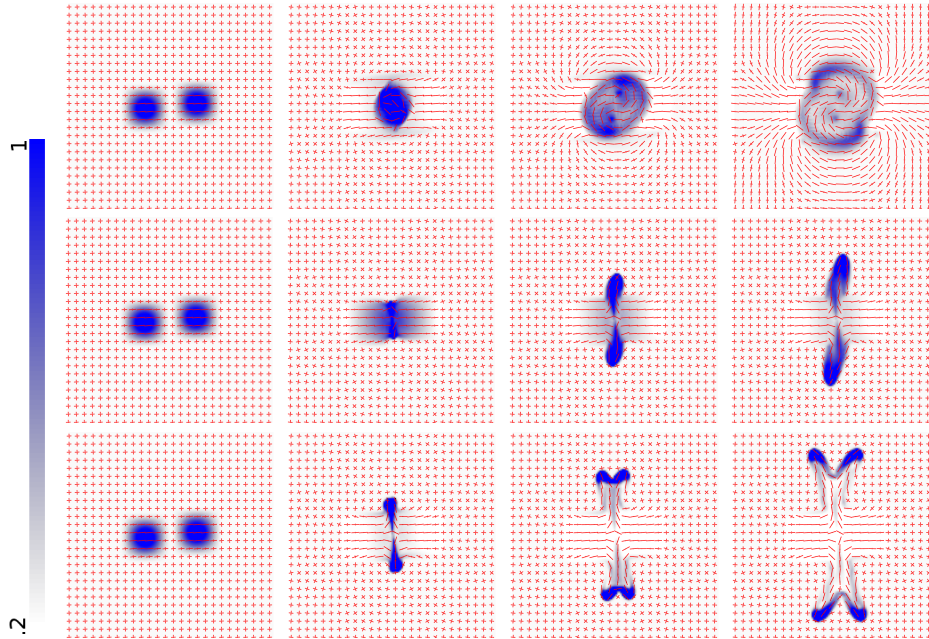


Fig. 14: Antiparallel colliding clump experiment with simplified motor model, $U_r = .001$ and $V_{sp} = 0$. First row: $C = 10$. Second row: $C = 50$. Third row: $C = 250$. First row images are at times $t=0, 300, 600, 900$ sec. Second row images are at times $t=0, 21, 42, 63$ sec. Third row images are at times $t=0, 15, 30, 45$ sec. See supplemental movie 4.

689 mental movie 5), we repeat the perturbation experiment with self-propulsion in the
 690 presence and absence of the hydrodynamic forces generated by the motor proteins.
 691 This allows us to test the observation of [28] that the stability and size of the observed
 692 filament patterns depend on long-range hydrodynamic interactions. Consistent with
 693 [28], we observe larger flow structures forming in a shorter amount of time in the pres-
 694 ence of the fluid flows driven by the motor proteins. We used the simplified motor
 695 model, $C = 100$, $U_r = .01$, and $V_{sp} = .1$.

696 **5. Conclusions.** We have developed a modeling and simulation framework cou-
 697 pling multiple microscopic models of propulsion to macroscopic steric and hydrody-
 698 namic interactions in a quasi-two-dimensional assay. Populations of bound and free
 699 motor proteins and microtubules are represented as continuum distributions. The
 700 framework facilitates study of the relative effects of hydrodynamic and steric interac-
 701 tions on emergent phenomena. Stress tensors arising from rotational and translational
 702 steric interactions and self-propulsion are supported in addition to body forces from
 703 active motor proteins. Experimentation is needed to empirically determine the steric
 704 interaction parameters U_r and U_x . We avoid closure approximations in the z dimen-
 705 sion, and high precision around a z -plane of interest is achieved without incurring
 706 significant computational overhead. Results demonstrate our framework's ability to
 707 replicate some of the behavior of individual and colliding clumps of filaments includ-
 708 ing crossovers, alignment, merging, and splitting [29], and support observations of [28]
 709 regarding hydrodynamic effects.

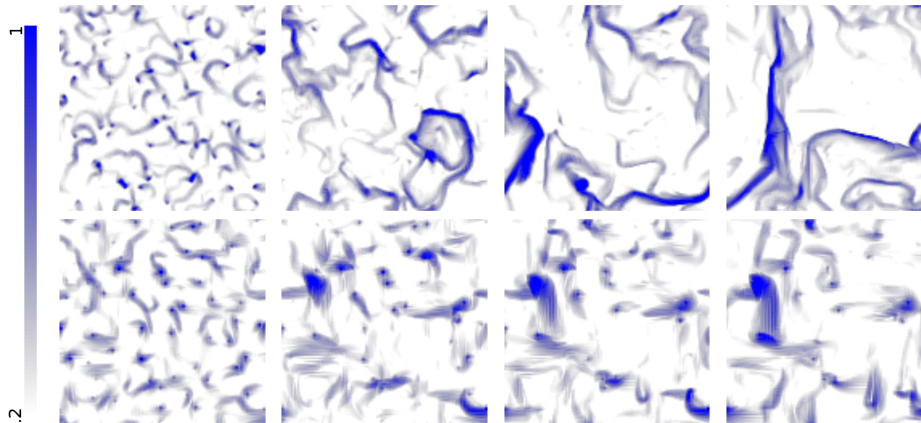


Fig. 15: Perturbation experiment with (first row) and without (second row) motor-based fluid forces, showing faster formation of larger-scale features in the former case. First row images are at times $t=150, 300, 450, 600$ sec. Second row images are at times $t=300, 600, 900, 1200$ sec. See supplemental movie 5.

710 We present two motor protein models, the evolved motor model which incorpo-
 711 rates motor head procession and binding/unbinding dynamics, and the simplified mo-
 712 tor model which determines the bound motor distribution instantaneously as a func-
 713 tion of the microtubule distribution, and therefore eliminates the high-dimensional
 714 and computationally expensive motor evolution at the smaller timescale t^* . While
 715 the different models may yield visually similar motor distributions, they can result in
 716 qualitatively different dynamics as illustrated in Figure 13. Additional motor mod-
 717 els could be investigated within our framework, for example, models accounting for
 718 cooperativity or competition between motor proteins. The framework could also be
 719 extended beyond gliding assays to support motor complexes directly linking micro-
 720 tubules as in [9].

721 Motor forces on the fluid compose flow features in the microtubule density by
 722 advecting all local microtubules with the same velocity. Even without any steric in-
 723 teraction terms, two colliding clumps will proceed in a direction roughly equal to
 724 the average of their orientations. However, the motor forces acting on the fluid are
 725 prone to cancellation in isotropic or anti-aligned microtubule configurations. Com-
 726 bining either motor model with a self-propulsion term in the microtubule advective
 727 flux provides a mechanism for anti-parallel sliding resulting in persistent motion of
 728 the microtubules. Addition of the self-propulsion term enables the passthrough of
 729 colliding clumps, consistent with the simulations of [29].

730 Acknowledgments.

731 REFERENCES

- 732 [1] I. S. ARANSON AND L. S. TSMIRING, *Pattern formation of microtubules and mo-*
 733 *tors: Inelastic interaction of polar rods*, Physical Review E, 71 (2005), p. 050901,
 734 [doi:10.1103/PhysRevE.71.050901](https://doi.org/10.1103/PhysRevE.71.050901), <http://dx.doi.org/10.1103/PhysRevE.71.050901>.
 735 [2] G. K. BATCHELOR, *The stress system in a suspension of force-free particles*, Journal of Fluid
 736 Mechanics, 41 (1970), pp. 545–570, [doi:10.1017/S0022112070000745](https://doi.org/10.1017/S0022112070000745), [http://dx.doi.org/10.](http://dx.doi.org/10.1017/S0022112070000745)
 737 [1017/S0022112070000745](http://dx.doi.org/10.1017/S0022112070000745).

- 738 [3] R. B. BIRD, C. F. CURTISS, R. C. ARMSTRONG, AND O. HASSAGER, *Dynamics of Polymeric*
739 *Liquids, Kinetic Theory*, Wiley-Interscience, volume 2 ed., June 1987, <http://www.amazon.com/exec/obidos/redirect?tag=citeulike07-20&path=ASIN/0471802441>.
- 740 [4] M. DOI AND S. F. EDWARDS, *The Theory of Polymer Dynamics*, Oxford University Press,
741 Oxford, 1986.
- 742 [5] K. DRESCHER, R. E. GOLDSTEIN, N. MICHEL, M. POLIN, AND I. TUVAL, *Direct measurement*
743 *of the flow field around swimming microorganisms*, Physical Review Letters, 105 (2010),
744 p. 168101.
- 745 [6] C. DULLEMOND, *Lecture on numerical fluid dynamics*. <http://www.mpia-hd.mpg.de/~dullemon/lectures/fluidynamics08>, 2008, <http://www.mpia-hd.mpg.de/~dullemon/lectures/fluidynamics08>.
- 746 [7] B. EZHILAN, M. J. SHELLEY, AND D. SAINTILLAN, *Instabilities and nonlinear dynamics of*
747 *concentrated active suspensions*, Physics of Fluids, 25 (2013), p. 070607.
- 748 [8] M. FRIGO AND S. G. JOHNSON, *Fftw: an adaptive software architecture for the fft*, in Acoustics,
749 Speech and Signal Processing, 1998. Proceedings of the 1998 IEEE International Conference
750 on, vol. 3, May 1998, pp. 1381–1384 vol.3, doi:10.1109/ICASSP.1998.681704.
- 751 [9] T. GAO, R. BLACKWELL, M. A. GLASER, M. BETTERTON, AND M. J. SHELLEY, *Multiscale*
752 *modeling and simulation of microtubule-motor-protein assemblies*, Physical Review E, 92
753 (2015), p. 062709.
- 754 [10] L. GIOMI, L. MAHADEVAN, B. CHAKRABORTY, AND M. F. HAGAN, *Excitable patterns in active*
755 *nematics*, Phys. Rev. Lett., 106 (2011), p. 218101, doi:10.1103/PhysRevLett.106.218101,
756 <http://link.aps.org/doi/10.1103/PhysRevLett.106.218101>.
- 757 [11] C. HOHENEGGER, S. COOK, AND T. SHINAR, *Dimensional Reduction of a Multiscale Continuum*
758 *Model of Microtubule Gliding Assays*, SIAM Journal on Applied Mathematics, 74 (2014),
759 pp. 1338–1353, doi:10.1137/140961535, <http://dx.doi.org/10.1137/140961535>.
- 760 [12] C. HOHENEGGER AND M. J. SHELLEY, *Dynamics of complex biofluids*, in New Trends in the
761 Physics and Mechanics of Biological Systems, M. Ben Amar, A. Goriely, M. M. Müller,
762 and L. F. Cugliandolo, eds., Ecole de Physique des Houches Session XCII, 6–31 July 2009,
763 Oxford University Press, 2011, ch. 3, pp. 65–92.
- 764 [13] J. HOWARD, *The movement of kinesin along microtubules*, Annual review of physiology, 58
765 (1996), pp. 703–729.
- 766 [14] J. KIERFELD, K. FRENTZEL, P. KRAIKIVSKI, AND R. LIPOWSKY, *Active dynamics of filaments in*
767 *motility assays*, The European Physical Journal-Special Topics, 157 (2008), pp. 123–133.
- 768 [15] P. KRAIKIVSKI, R. LIPOWSKY, AND J. KIERFELD, *Enhanced ordering of interact-*
769 *ing filaments by molecular motors*, Phys. Rev. Lett., 96 (2006), p. 258103,
770 doi:10.1103/PhysRevLett.96.258103, <http://link.aps.org/doi/10.1103/PhysRevLett.96.258103>.
- 771 [16] H. Y. LEE AND M. KARDAR, *Macroscopic equations for pattern formation in mixtures*
772 *of microtubules and molecular motors*, Physical Review E, 64 (2001), p. 056113,
773 doi:10.1103/PhysRevE.64.056113, <http://dx.doi.org/10.1103/PhysRevE.64.056113>.
- 774 [17] T. B. LIVERPOOL, *Active gels: where polymer physics meets cytoskeletal dynamics*, Philosophical
775 Transactions of the Royal Society of London A: Mathematical, Physical and Engineering
776 Sciences, 364 (2006), pp. 3335–3355.
- 777 [18] T. B. LIVERPOOL AND M. C. MARCHETTI, *Bridging the microscopic and the hydro-*
778 *dynamic in active filament solutions*, Europhysics Letters, 69 (2005), pp. 846–852,
779 doi:10.1209/epl/i2004-10414-0, <http://dx.doi.org/10.1209/epl/i2004-10414-0>.
- 780 [19] F. NÉDÉLEC, *Computer simulations reveal motor properties generating stable antipar-*
781 *allel microtubule interactions*, The Journal of Cell Biology, 158 (2002), pp. 1005–1015,
782 doi:10.1083/jcb.200202051, <http://dx.doi.org/10.1083/jcb.200202051>.
- 783 [20] F. NÉDÉLEC AND D. FOETHKE, *Collective langevin dynamics of flexible cytoskeletal fibers*, New
784 Journal of Physics, 9 (2007), p. 427, doi:10.1088/1367-2630/9/11/427, <http://dx.doi.org/10.1088/1367-2630/9/11/427>.
- 785 [21] F. NÉDÉLEC, T. SURREY, AND A. C. MAGGS, *Dynamic concentration of mo-*
786 *tors in microtubule arrays*, Physical Review Letters, 86 (2001), pp. 3192–3195,
787 doi:10.1103/PhysRevLett.86.3192, <http://dx.doi.org/10.1103/PhysRevLett.86.3192>.
- 788 [22] F. J. NÉDÉLEC AND T. SURREY, *Dynamics of microtubule aster formation by motor complexes*,
789 Comptes-Rendus de l’Académie des Sciences Paris, 4 (2001), pp. 841–847.
- 790 [23] C. PESKIN, *The immersed boundary method*, Acta Numerica, 11 (2003), pp. 479–517,
791 doi:10.1017/S0962492902000077, <http://dx.doi.org/10.1017/S0962492902000077>.
- 792 [24] S. L. ROGERS AND J. M. SCHOLEY, *Motility assays for microtubule motor proteins*, Nature
793 Encyclopedia of Life Sciences, (2001), doi:10.1038/npg.els.0002621, <http://dx.doi.org/10.1038/npg.els.0002621>.
- 794
795
796
797
798
799

- 800 [25] D. SAINTILLAN AND M. J. SHELLEY, *Instabilities and pattern formation in active particle sus-*
801 *sensions: Kinetic theory and continuum simulations*, Physical review letters, 100 (2008),
802 p. 178103, doi:10.1103/PhysRevLett.100.178103.
- 803 [26] D. SAINTILLAN AND M. J. SHELLEY, *Instabilities, pattern formation, and mixing in active*
804 *suspensions*, Physics of Fluids, 20 (2008), pp. 123304+, doi:10.1063/1.3041776, http://dx.
805 doi.org/10.1063/1.3041776.
- 806 [27] S. SANKARARAMAN, G. I. MENON, AND P. B. SUNILKUMAR, *Self-organized pattern for-*
807 *mation in motor-microtubule mixtures*, Physical Review E, 70 (2004), p. 031905,
808 doi:10.1103/PhysRevE.70.031905, http://dx.doi.org/10.1103/PhysRevE.70.031905.
- 809 [28] V. SCHALLER, C. WEBER, E. FREY, AND A. R. BAUSCH, *Polar pattern formation:*
810 *hydrodynamic coupling of driven filaments*, Soft Matter, 7 (2011), pp. 3213–3218,
811 doi:10.1039/C0SM01063D, http://dx.doi.org/10.1039/C0SM01063D.
- 812 [29] V. SCHALLER, C. WEBER, C. SEMMRICH, W. FREY, AND A. R. BAUSCH, *Polar patterns of*
813 *driven filaments*, Nature, 467 (2010), pp. 73–77, doi:10.1038/nature09312, http://dx.doi.
814 org/10.1038/nature09312.
- 815 [30] M. J. SHELLEY, *The dynamics of microtubule/motor-protein assemblies in biology and physics*,
816 Annual Review of Fluid Mechanics, 48 (2016), pp. 487–506.
- 817 [31] T. SHINAR, M. MANA, F. PIANO, AND M. J. SHELLEY, *A model of cytoplasmically driven*
818 *microtubule-based motion in the single-celled caenorhabditis elegans embryo*, Proceedings
819 of the National Academy of Sciences, 108 (2011), pp. 10508–10513.
- 820 [32] Y. SUMINO, K. H. NAGAI, Y. SHITAKA, D. TANAKA, K. YOSHIKAWA, H. CHATE, AND K. OIWA,
821 *Large-scale vortex lattice emerging from collectively moving microtubules*, Nature, 483
822 (2012), pp. 448–452, doi:10.1038/nature10874, http://dx.doi.org/10.1038/nature10874.
- 823 [33] S. SWAMINATHAN, F. ZIEBERT, D. KARPEEV, AND I. S. ARANSON, *Motor-mediated align-*
824 *ment of microtubules in semidilute mixtures*, Physical Review E, 79 (2009), p. 036207,
825 doi:10.1103/PhysRevE.79.036207, http://dx.doi.org/10.1103/PhysRevE.79.036207.
- 826 [34] Q. WANG, *A hydrodynamic theory for solutions of nonhomogeneous nematic liquid crystalline*
827 *polymers of different configurations*, The Journal of chemical physics, 116 (2002), pp. 9120–
828 9136.